NASA/TM—2010-216323

A Nonlinear Dynamic Subscale Model for Partially Resolved Numerical Simulation (PRNS)/Very Large Eddy Simulation (VLES) of Internal Non-Reacting Flows

Tsan-Hsing Shih
Ohio Aerospace Institute, Brook Park, Ohio

Nan-Suey Liu
Glenn Research Center, Cleveland, Ohio

May 2010

NASA STI Program . . . in Profile

Since its founding, NASA has been dedicated to the advancement of aeronautics and space science. The NASA Scientific and Technical Information (STI) program plays a key part in helping NASA maintain this important role.

The NASA STI Program operates under the auspices of the Agency Chief Information Officer. It collects, organizes, provides for archiving, and disseminates NASA's STI. The NASA STI program provides access to the NASA Aeronautics and Space Database and its public interface, the NASA Technical Reports Server, thus providing one of the largest collections of aeronautical and space science STI in the world. Results are published in both non-NASA channels and by NASA in the NASA STI Report Series, which includes the following report types:

- TECHNICAL PUBLICATION. Reports of completed research or a major significant phase of research that present the results of NASA programs and include extensive data or theoretical analysis. Includes compilations of significant scientific and technical data and information deemed to be of continuing reference value. NASA counterpart of peer-reviewed formal professional papers but has less stringent limitations on manuscript length and extent of graphic presentations.

- TECHNICAL MEMORANDUM. Scientific and technical findings that are preliminary or of specialized interest, e.g., quick release reports, working papers, and bibliographies that contain minimal annotation. Does not contain extensive analysis.

- CONTRACTOR REPORT. Scientific and technical findings by NASA-sponsored contractors and grantees.

- CONFERENCE PUBLICATION. Collected papers from scientific and technical conferences, symposia, seminars, or other meetings sponsored or cosponsored by NASA.

- SPECIAL PUBLICATION. Scientific, technical, or historical information from NASA programs, projects, and missions, often concerned with subjects having substantial public interest.

- TECHNICAL TRANSLATION. English-language translations of foreign scientific and technical material pertinent to NASA's mission.

Specialized services also include creating custom thesauri, building customized databases, organizing and publishing research results.

For more information about the NASA STI program, see the following:

- Access the NASA STI program home page at *http://www.sti.nasa.gov*

- E-mail your question via the Internet to *help@sti.nasa.gov*

- Fax your question to the NASA STI Help Desk at 443–757–5803

- Telephone the NASA STI Help Desk at 443–757–5802

- Write to:
  NASA Center for AeroSpace Information (CASI)
  7115 Standard Drive
  Hanover, MD 21076–1320

NASA/TM—2010-216323

A Nonlinear Dynamic Subscale Model for Partially Resolved Numerical Simulation (PRNS)/Very Large Eddy Simulation (VLES) of Internal Non-Reacting Flows

Tsan-Hsing Shih
Ohio Aerospace Institute, Brook Park, Ohio

Nan-Suey Liu
Glenn Research Center, Cleveland, Ohio

National Aeronautics and
Space Administration

Glenn Research Center
Cleveland, Ohio 44135

May 2010

Acknowledgments

This work was supported by the Subsonics Fixed Wing Project as part of the NASA Fundamental Aeronautics Program. The authors would like to thank Dr. Farhad Davoudzadeh for providing the numerical grid of the single-element LDI combustor.

This report is a formal draft or working paper, intended to solicit comments and ideas from a technical peer group.

This report contains preliminary findings, subject to revision as analysis proceeds.

This work was sponsored by the Fundamental Aeronautics Program at the NASA Glenn Research Center.

Level of Review: This material has been technically reviewed by technical management.

Available from

NASA Center for Aerospace Information
7115 Standard Drive
Hanover, MD 21076–1320

National Technical Information Service
5301 Shawnee Road
Alexandria, VA 22312

Available electronically at http://gltrs.grc.nasa.gov

Contents

A Nonlinear Dynamic Subscale Model for Partially Resolved Numerical Simulation (PRNS)/Very Large Eddy Simulation (VLES) of Internal Non-Reacting Flows

Tsan-Hsing Shih
Ohio Aerospace Institute
Brook Park, Ohio 44142

Nan-Suey Liu
National Aeronautics and Space Administration
Glenn Research Center
Cleveland, Ohio 44135

Abstract

A brief introduction of the temporal filter based partially resolved numerical simulation/very large eddy simulation approach (PRNS/VLES) and its distinct features are presented. A nonlinear dynamic subscale model and its advantages over the linear subscale eddy viscosity model are described. In addition, a guideline for conducting a PRNS/VLES simulation is provided. Results are presented for three turbulent internal flows. The first one is the turbulent pipe flow at low and high Reynolds numbers to illustrate the basic features of PRNS/VLES; the second one is the swirling turbulent flow in a LM6000 single injector to further demonstrate the differences in the calculated flow fields resulting from the nonlinear model versus the pure eddy viscosity model; the third one is a more complex turbulent flow generated in a single-element lean direct injection (LDI) combustor, the calculated result has demonstrated that the current PRNS/VLES approach is capable of capturing the dynamically important, unsteady turbulent structures while using a relatively coarse grid.

1.0 Introduction

Many engineering applications of the computational fluid dynamics (CFD) for combustor flows need to capture the relatively large scales of unsteady, turbulent structures at both low and high Reynolds numbers to facilitate a higher fidelity analysis of the design. The conventional Reynolds-averaged Navier-Stokes (RANS) approach is known to be limited for this kind of task, because, by definition, the RANS solution can not contain the abovementioned flow information. Most recently, an approach called partially resolved numerical simulation (PRNS) (Refs. 1 and 2) has been developed for the simulation of very large eddy turbulence while using RANS type of grid resolution. Although PRNS is mainly aimed at the very large eddy simulation (VLES), hence notated as PRNS/VLES, it can easily be set to perform the large eddy simulation (LES) when the grid spacing reaches the traditional LES type of resolution. PRNS/VLES is based on the concept of temporal filtering to avoid the frequently overlooked issues that the traditional LES approach suffers from when a spatial filter is employed in conjunction with a spatially non-uniform grid. In PRNS/VLES, the larger time scales (or lower frequencies) of the turbulence are directly calculated, and the effects of the unresolved time scales of the turbulence are modeled by a dynamic equation system. The contents of both the resolved and unresolved turbulence are regulated by a "resolution control parameter" (RCP), which is related to the width of the temporal filter.

The basic equations of PRNS/VLES and its subscale models are grid invariant, i.e., they do not have grid spacing as a parameter in their formal formulations. Therefore, it is possible to achieve a grid-independent numerical solution, and this is a major difference from the traditional LES approach and its variants. Another distinction is that PRNS/VLES enables us to perform unsteady RANS (URANS), VLES, LES, and even DNS in a unified way through the judicious selection of the value of RCP, in

conjunction with the employment of a grid spacing whose numerical resolution can consistently support the scale contents stipulated by the selected RCP. It should be noted that the PRNS/VLES approach is not a variant of the popular hybrid RANS/LES (Refs. 3, 4, 5, and 6). There is no enforced transition between the perceived RANS and LES domains.

The subscale model is always one of the key issues in all turbulent numerical simulations. Some less than satisfactory large eddy simulations using the Smagorinsky eddy viscosity and its variants have been reported in the past (Refs. 7 and 8). Recently, we have also noticed that in a PRNS/VLES calculation of the turbulent pipe flow at a low Reynolds number $\mathrm{Re}_\tau = 180$ (based on the pipe radius and the skin friction velocity), the turbulent fluctuations were not sustainable over a long period of time and were eventually suppressed; and this can be attributed to the attempt of just using the eddy viscosity to account for all the subscale effects, even though the eddy viscosity is constructed from a $k-\varepsilon$ dynamic equation system. It is known that, in addition to the dissipative and diffusive effects accounted for through the eddy viscosity, the effects of anisotropy and rotation should also be included in the subscale model, especially when the simulation is a very large eddy simulation. To construct a more general relationship between the unresolved turbulent stresses and the resolved turbulent flow field, we have followed the analysis of the rational mechanics and obtained a general constitutive relationship (Refs. 9 and 10). This relationship indeed shows that, in addition to an eddy-viscosity term, there are several other terms representing the anisotropy and the rotation effects due to the interactions between the resolved and unresolved turbulence. They then introduce source terms in the momentum equation to sustain the turbulent fluctuations in the calculated flow field. The simulations presented in this paper will demonstrate this unique feature of the nonlinear subscale model.

In the following, a brief description of the PRNS/VLES equations and the subscale model will first be presented, followed by an outline for the concurrent selections of RCP and the numerical grid. The results of simulations from three internal turbulent flows are then presented: the turbulent pipe flow, the turbulent swirling flow issued from a LM6000 single injector, and the flow generated in a single element lean direct injection (LDI) combustor.

2.0 Temporal Filter Based PRNS/VLES Approach

Using a homogeneous temporal filter $G(t-t')$, the large time-scale turbulent variable $\bar{\phi}$ and its density-weighted variable $\tilde{\phi}$ can be defined as

$$\bar{\phi}(t,x_i) = \int \phi(t',x_i)\,G(t-t')\,dt', \quad \tilde{\phi} = \frac{\overline{\rho\phi}}{\bar{\rho}}, \tag{1}$$

where the integral is over the entire time domain and G satisfies the normalization condition: $\int G(t-t')\,dt' = 1$. There are several such temporal filters available, the simplest one is the top hat filter:

$$G(t-t') = \begin{cases} 1/\Delta_T, & \text{if } |t-t'| \le \Delta_T/2 \\ 0, & \text{otherwise} \end{cases}, \tag{2}$$

where Δ_T is the width of the top hat filter. Using this filter, the left part of Equation (1) becomes

$$\bar{\phi}(t,x_i) = \frac{1}{\Delta_T}\int_{t-\Delta_T/2}^{t+\Delta_T/2} \phi(t',x_i)\,dt'. \tag{3}$$

Equation (3) reveals an unified feature of $\overline{\phi}$ and $\tilde{\phi}$, because they will become the exact Reynolds-averaged quantity and Favre-averaged quantity when $\Delta_T \to \infty$. On the other hand, they will become the instantaneous turbulent quantity as $\Delta_T \to 0$. For a finite Δ_T, they represent the quantities of large time-scale turbulence.

2.1 Basic Equation

Performing the filtering operation defined by Equation (1) on the Navier-Stokes equations, we obtain a set of exact, basic equations for the resolved, large time-scale turbulence ($\overline{\phi}$ and $\tilde{\phi}$):

$$\left(\overline{\rho}\tilde{u}_i\right)_{,t} + \left(\overline{\rho}\tilde{u}_i\tilde{u}_j\right)_{,j} = -\overline{p}_{,i} - \tau_{ij,j} + \left(2\overline{\mu}\tilde{s}_{ij} - \frac{2}{3}\delta_{ij}\overline{\mu}\tilde{s}_{kk}\right)_{,j}, \tag{4}$$

$$\left(\overline{\rho}\tilde{e}\right)_{,t} + \left(\overline{\rho}\tilde{u}_i\tilde{e}\right)_{,i} = \left(\overline{\kappa}\tilde{T}_{,i}\right)_{,i} + \overline{ps_{kk}} - q_{i,i} + \left(2\overline{\mu}\widetilde{s_{ij}s_{ij}} - \frac{2}{3}\overline{\mu}\widetilde{s_{kk}s_{ii}}\right) + \overline{Q}, \tag{5}$$

$$\overline{\rho}_{,t} + \left(\overline{\rho}\tilde{u}_i\right)_{,i} = 0, \quad \overline{p} = \overline{\rho}R\tilde{T}, \tag{6}$$

$$\tau_{ij} \equiv \overline{\rho}(\widetilde{u_iu_j} - \tilde{u}_i\tilde{u}_j), \quad q_i \equiv \overline{\rho}(\widetilde{u_ie} - \tilde{u}_i\tilde{e}). \tag{7}$$

where $s_{ij} = \left(u_{i,j} + u_{j,i}\right)/2$. The symbols $(\,)_{,t}$ and $(\,)_{,i}$ represent the temporal and spatial derivatives, respectively. ρ, u_i, T, p, e, and Q are the density, velocity, temperature, pressure, internal energy per unit mass, and the radiation rate. μ and κ are the viscosity and heat conductivity of the fluid. R is the gas constant. τ_{ij} and q_i are the extra terms that were created by the process of temporally filtering the nonlinear Navier-Stokes equations. They represent the effects of unresolved, small time-scale turbulence. However, they are not in closed forms, and must be modeled. We call them the unresolved turbulent stresses and heat fluxes.

It is clear that the basic Equations (4) to (7) which govern the large time-scale turbulence are not associated with the grid spacing, hence they are grid independent or grid invariant. This feature must be maintained in the development of the subscale models. It is important to note that in the temporally filtered turbulent field the filtering time scale Δ_T is not the sole factor in determining the effective filtering length scale of the numerical simulation, and this gives leeway in arranging the grid spacing to carry out a physically meaningful numerical simulation.

2.2 Nonlinear Subscale Model

In order to obtain the solution for the large time-scale turbulence using PRNS/VLES Equations (4) to (6), we must model the unclosed terms defined in Equation (7): $\tau_{ij} \equiv \overline{\rho}(\widetilde{u_iu_j} - \tilde{u}_i\tilde{u}_j)$, $q_i \equiv \overline{\rho}(\widetilde{u_ie} - \tilde{u}_i\tilde{e})$. There are several ways to model these terms. The more sophisticated method is to directly solve the transport equations for the unresolved turbulent stresses and heat fluxes, which can be derived from the Navier-Stokes equations (see Ref. 1). This method will require modeling of higher order unclosed terms appeared in the transport equation system of τ_{ij} and q_i. A less complicated way is to use a general constitutive relationship between the unresolved turbulent stresses τ_{ij} and the strain rate of resolved large time-scale turbulence $\tilde{s}_{ij}$, $\tilde{\omega}_{ij}$. This general constitutive relationship is then simplified according to the flow complexity by truncating the higher order nonlinear terms of $\tilde{s}_{ij}$, $\tilde{\omega}_{ij}$. For example, the simplest form is just a linear relationship, which is the widely used subscale eddy viscosity model. Even at this

level, there are several ways to formulate the subscale eddy viscosity. The most popular one used in the traditional LES is the Smagorinsky model (Ref. 11) and its variations, which explicitly uses the local grid spacing Δ as the filtering length scale. A more sophisticated one is the one-equation model, such as the one proposed by Kim and Menon (Ref. 12), which solves the transport equation of the unresolved turbulent kinetic energy k, and using $\sqrt{k}$ as the velocity scale, but still keeping the local grid spacing as the filtering length scale.

In the context of PRNS/VLES, the subscale model is required to be a function of the width of the temporal filter Δ_T, but independent of the local grid spacing. The constitutive relationship for the unresolved turbulent stresses is derived from the general constitutive relationship (Ref. 13) by invoking the realizability condition and the rapid distortion theory limit. The current subscale model contains linear, quadratic and cubic terms while the temporal filter width Δ_T appears via the resolution control parameter RCP.

2.2.1 Modeling of Unresolved Turbulent Stresses τ_{ij}

The model proposed for PRNS/VLES is the following:

$$\begin{aligned}\tau_{ij} = &-2f_1 C_\mu \bar{\rho}\frac{k^2}{\varepsilon}\left(\tilde{s}_{ij} - \delta_{ij}\tilde{s}_{kk}/3\right) + \frac{1}{3}\delta_{ij}\tau_{kk} \\ &- A_3 f_3 \bar{\rho}\frac{k^3}{\varepsilon^2}\left(\tilde{s}_{ik}\tilde{\omega}_{kj} - \tilde{\omega}_{ik}\tilde{s}_{kj}\right) \\ &+ 2A_5 f_5 \bar{\rho}\frac{k^4}{\varepsilon^3}\left[\tilde{\omega}_{ik}\tilde{s}_{kj}^2 - \tilde{s}_{ik}^2\tilde{\omega}_{kj} + \tilde{\omega}_{ik}\tilde{s}_{km}\tilde{\omega}_{mj} - \tilde{\omega}_{kl}\tilde{s}_{lm}\tilde{\omega}_{mk}\delta_{ij} + II_s(\tilde{s}_{ij} - \delta_{ij}\tilde{s}_{kk}/3)\right],\end{aligned} \tag{8}$$

where, $\tilde{s}_{ij} = \left(\tilde{u}_{i,j} + \tilde{u}_{j,i}\right)/2$, $\tilde{\omega}_{ij} = \left(\tilde{u}_{i,j} - \tilde{u}_{j,i}\right)/2$, $II_s = \left(\tilde{s}_{kk}\tilde{s}_{mm} - \tilde{s}_{kl}\tilde{s}_{lk}\right)/2$. The model coefficients C_μ, A_3 and A_5 are constrained by the realizability condition and the rapid distortion theory limit. They are not arbitrary but formulated as (see Ref. 13):

$$C_\mu = \frac{1}{4.0 + A_s\dfrac{k}{\varepsilon}U^*}, \quad A_3 = \frac{\sqrt{1.0 - A_s^2 C_\mu^2\left(\dfrac{k}{\varepsilon}S^*\right)^2}}{0.5 + 1.5\dfrac{k^2}{\varepsilon^2}\Omega^* S^*}, \quad A_5 = \frac{1.6\,C_\mu\bar{\rho}\dfrac{k^2}{\varepsilon}}{\bar{\rho}\dfrac{k^4}{\varepsilon^3}\dfrac{7S^*S^* + \Omega^*\Omega^*}{4}}, \tag{9}$$

in which,

$$A_s = \sqrt{6}\cos\varphi, \quad \varphi = \frac{1}{3}\arccos\left(\sqrt{6}W^*\right), \quad W^* = \frac{S_{ij}^* S_{jk}^* S_{ki}^*}{(S^*)^3}, \tag{10}$$

$$U^* = \sqrt{(S^*)^2 + (\Omega^*)^2}, \quad S^* = \sqrt{S_{ij}^* S_{ij}^*}, \quad \Omega^* = \sqrt{\omega_{ij}\omega_{ij}}, \quad S_{ij}^* = \tilde{s}_{ij} - \frac{1}{3}\delta_{ij}\tilde{s}_{kk} \tag{11}$$

The coefficients f_1, f_3, and f_5 are functions of Δ_T/T, i.e. the ratio of the temporal filter width to the global time scale of the turbulent flow of interest, where the global time scale T can be considered as the maximum integral time scale in the entire domain. These functions must have the following property:

$$f_i\left(\frac{\Delta_T}{T}\right)=\begin{cases}0 & \text{if } \dfrac{\Delta_T}{T}\to 0\,,\\ 1 & \text{if } \dfrac{\Delta_T}{T}\to 1\,.\end{cases} \tag{12}$$

This is because the unresolved turbulent stresses τ_{ij} must vanish when the filter width Δ_T vanishes, and τ_{ij} must approach the Reynolds-averaged stresses R_{ij} as Δ_T increases towards the global time scale T. In PRNS/VLES, $\Delta_T/T<1$, so we may take the following general expansion:

$$f_i\left(\frac{\Delta_T}{T}\right)=C_0^i+C_1^i\left(\frac{\Delta_T}{T}\right)+C_2^i\left(\frac{\Delta_T}{T}\right)^2+\cdots \qquad i=1,3,5. \tag{13}$$

All C_0^i must be zero, because f_i must be zero as Δ_T goes to zero. If we retain the remaining two leading terms as an approximation and assume the first order derivative of f_i is zero at $\Delta_T/T=1$ to reflect that f_i reaches its maximum value of 1.0 at $\Delta_T/T=1$, then all f_i will have the same form:

$$f_i\left(\frac{\Delta_T}{T}\right)\approx 2\left(\frac{\Delta_T}{T}\right)-\left(\frac{\Delta_T}{T}\right)^2 \qquad i=1,3,5 \tag{14}$$

We call the ratio Δ_T/T the resolution control parameter (RCP). It controls, at the governing equation level, the content of resolved large time-scale turbulence in the resolved field, which may, in theory, contain all length scales that have not been physically filtered. However, at the numerical solution level, the grid spacing will be imposed and its associated solution (say, the subscale eddy viscosity) together with the RCP will determine the effective content of the large-length scale turbulence. We will further discuss this parameter in Section 2.4.1.

2.2.2 Nonlinear Interaction Between Resolved and Unresolved Turbulence

It is important to identify the various physical interactions between the resolved and unresolved turbulent scales and to understand how these interactions are mimicked in the numerical simulation. In the momentum equation (4), these interactions are represented by the term $\tau_{ij,j}$, which is unclosed and must be modeled. In the traditional LES, this term is modeled via the isotropic eddy viscosity. Therefore, the effect of the interactions is accounted for only by a modification to the viscosity of the fluid. However, the real physical interactions are much more complex than this. In fact, the general constitutive relationship of τ_{ij} contains many more terms, in addition to a leading term that is related to an eddy viscosity. For example, the model of τ_{ij} in Equation (8) has two parts: the linear term and the nonlinear (quadratic and cubic) terms. Each part plays different role in the momentum equation. The linear part leads to a term acting like an additional viscosity (called the subscale eddy viscosity); and the nonlinear part leads to terms acting like additional sources capable of promoting the resolved large scale turbulence. This can be clearly demonstrated by plugging the τ_{ij} model into Equation (4), which yields

$$\left(\bar{\rho}\tilde{u}_i\right)_{,t}+\left(\bar{\rho}\tilde{u}_i\tilde{u}_j\right)_{,j}=-\left(\bar{p}+\frac{1}{3}\tau_{kk}\right)_{,i}+\left(2\left(\bar{\mu}+\mu_T\right)\tilde{s}_{ij}-\frac{2}{3}\delta_{ij}\left(\bar{\mu}+\mu_T\right)\tilde{s}_{kk}\right)_{,j}+S_i^T\,, \tag{15}$$

where,

$$\mu_T=f_1 C_\mu \bar{\rho}\frac{k^2}{\varepsilon} \tag{16}$$

$$S_i^T = \left\{ A_3 f_3 \bar{\rho} \frac{k^3}{\varepsilon^2} \left(\tilde{s}_{ik} \tilde{\omega}_{kj} - \tilde{\omega}_{ik} \tilde{s}_{kj} \right) \right\}_{,j} - \left\{ 2A_5 f_5 \bar{\rho} \frac{k^4}{\varepsilon^3} \left[\tilde{\omega}_{ik} \tilde{s}_{kj}^2 - \tilde{s}_{ik}^2 \tilde{\omega}_{kj} + \tilde{\omega}_{ik} \tilde{s}_{km} \tilde{\omega}_{mj} - \tilde{\omega}_{kl} \tilde{s}_{lm} \tilde{\omega}_{mk} \delta_{ij} + II_s (\tilde{s}_{ij} - \delta_{ij} \tilde{s}_{kk} / 3) \right] \right\}_{,j} \tag{17}$$

Apparently, the linear part of the model adds an additional subscale eddy viscosity μ_T (which is isotropic) to the viscosity of the fluid $\bar{\mu}$; and the nonlinear part provides a complex source term S_i^T, which accounts for the effects of anisotropy and rotation.

We have noticed that, although different subscale eddy viscosity models have been used in different LES approaches, most of them have neglected or missed the source term S_i^T. Our study shows that this source term could become critically important for some flow simulations, especially for those at relatively low Reynolds numbers or flows with strong rotation, and this will be demonstrated in Section 3.1.1.2 and Section 3.2.2.

2.2.3 Transport Equations for Subscale k – ε

To complete the proposed model for τ_{ij}, we need k and ε, the unresolved turbulent kinetic energy and its dissipation rate. Their exact transport equations can be derived from the Navier-Stokes equations, and contain several higher order unclosed terms due to the temporal filtering operation. Here, we briefly describe the procedure of the derivation. The first step is to establish the transport equation for τ_{ij}, followed by a tracing operation to establish the equation for τ_{ii} (which is $2\bar{\rho}k$), and this leads to the transport equation for k.

The exact transport equation for the unresolved turbulent stresses $\tau_{ij} = (\widetilde{\bar{\rho} u_i u_j} - \bar{\rho} \tilde{u}_i \tilde{u}_j)$ is

$$\tau_{ij,t} + \left(\tilde{u}_k \tau_{ij} \right)_{,k} = D_{ij} + \Phi_{ij} + P_{ij} - \bar{\rho} \varepsilon_{ij} , \tag{18}$$

where D_{ij}, Φ_{ij}, P_{ij} and $\bar{\rho}\varepsilon_{ij}$ are the diffusion term, the pressure-strain correlation term, the production term, and the dissipation term, respectively. The following expressions indicate that all terms on the right hand side of the equation, except for the production term P_{ij}, are unclosed and must be modeled.

$$D_{ij} = -\left(\bar{\rho} \widetilde{u_i u_j u_k} - \bar{\rho} \widetilde{u_i u_j} \tilde{u}_k \right) + \left\{ 2\bar{\mu} \widetilde{u_j s_{ik}} - \frac{2}{3} \delta_{ik} \bar{\mu} \widetilde{u_j s_{mm}} - \left[\widetilde{u_j} \left(2\bar{\mu} \tilde{s}_{ik} - \frac{2}{3} \delta_{ik} \bar{\mu} \tilde{s}_{mm} \right) \right] \right\}_{,k}$$
$$+ \left(\tau_{ik} \tilde{u}_j + \tau_{jk} \tilde{u}_i \right)_{,k} - \left(\overline{p u_j} \delta_{ik} + \overline{p u_i} \delta_{jk} - \bar{p} \tilde{u}_j \delta_{ik} - \bar{p} \tilde{u}_i \delta_{jk} \right)_{,k}$$
$$+ \left\{ 2\bar{\mu} \widetilde{u_i s_{jk}} - \frac{2}{3} \delta_{jk} \bar{\mu} \widetilde{u_i s_{mm}} - \left[\tilde{u}_i \left(2\bar{\mu} \tilde{s}_{jk} - \frac{2}{3} \delta_{jk} \bar{\mu} \tilde{s}_{mm} \right) \right] \right\}_{,k}$$

$$\Phi_{ij} = 2\overline{p s_{ij}} - 2\bar{p} \tilde{s}_{ij}$$

$$P_{ij} = -\tau_{ik} \tilde{u}_{j,k} - \tau_{jk} \tilde{u}_{i,k}$$

$$\bar{\rho} \varepsilon_{ij} = \left[2\bar{\mu} \left(\widetilde{s_{ik} u_{j,k}} + \widetilde{s_{jk} u_{i,k}} \right) - \frac{4}{3} \bar{\mu} \widetilde{s_{mm} s_{ij}} \right] - \left[2\bar{\mu} \left(\tilde{s}_{ik} \tilde{u}_{j,k} + \tilde{s}_{jk} \tilde{u}_{i,k} \right) - \frac{4}{3} \bar{\mu} \tilde{s}_{mm} \tilde{s}_{ij} \right].$$

Now, if the diffusion term D_{ij} is modeled by a gradient-type diffusion of τ_{ij} with the effective viscosity, $\bar{\mu} + \mu_T$, then the trace of Equation (18) becomes

$$\frac{\partial}{\partial t}\bar{\rho}k + \frac{\partial}{\partial x_i}\bar{\rho}\tilde{u}_i k = \frac{\partial}{\partial x_i}\left[\left(\bar{\mu} + \mu_T\right)\frac{\partial}{\partial x_i}k\right] - \tau_{ij}\tilde{s}_{ij} - \bar{\rho}\varepsilon \tag{19}$$

in which, Φ_{ii} has been neglected by ignoring the effect of compressibility on Φ_{ij}.

The dissipation rate is defined by $\bar{\rho}\varepsilon_{ii}/2$, i.e.,

$$\bar{\rho}\varepsilon = \left(2\bar{\mu}\widetilde{s_{ij}s_{ij}} - \frac{2}{3}\bar{\mu}\widetilde{s_{mm}s_{ii}}\right) - \left(2\bar{\mu}\tilde{s}_{ij}\tilde{s}_{ij} - \frac{2}{3}\bar{\mu}\widetilde{s_{mm}}\,\widetilde{s_{ii}}\right) \tag{20}$$

A model transport equation for the dissipation rate ε can be constructed by the analogy to Equation (19) as

$$\frac{\partial}{\partial t}\bar{\rho}\varepsilon + \frac{\partial}{\partial x_i}\bar{\rho}\tilde{u}_i \varepsilon = \frac{\partial}{\partial x_i}\left[\left(\bar{\mu} + \mu_T\right)\frac{\partial}{\partial x_i}\varepsilon\right] - C_{\varepsilon 1}\tau_{ij}\tilde{s}_{ij}\frac{\varepsilon}{k} - C_{\varepsilon 2}\frac{\bar{\rho}\varepsilon^2}{k} \tag{21}$$

where $C_{\varepsilon 1}$ and $C_{\varepsilon 2}$ are the model coefficients. We have adopted the commonly used values of $C_{\varepsilon 1} = 1.45$ and $C_{\varepsilon 2} = 1.92$ in the present work; while keeping in mind that they can be further constructed as functions of the local subscale turbulence quantities (Ref. 14).

2.2.4 Modeling of Unresolved Turbulent Heat Fluxes q_i

A common practice in modeling the unresolved turbulent heat fluxes $q_i \equiv \bar{\rho}(\widetilde{u_i e} - \tilde{u}_i\tilde{e})$ is to employ the following isotropic model:

$$q_i = -\kappa_T \tilde{e}_{,i} \tag{22}$$

where κ_T is the eddy diffusivity for the heat, which is often modeled as $\kappa_T = \mu_T / \mathrm{Pr}_T$, where Pr_T (about 0.9) is the turbulent Prandtl number. However, based on the analysis of the constitutive relationship (see Ref. 9 and 10), the simplest form that considers the effects of strain and rotation should be

$$q_i = -\kappa_T \tilde{e}_{,i} - \kappa_T \frac{k}{\varepsilon}\left(c_1\tilde{s}_{ij} + c_2\tilde{\omega}_{ij}\right)\tilde{e}_{,j} \tag{23}$$

Where c_1 and c_2 are yet to be determined coefficients. This more general model will result in modifications to both the diffusion term and the source term in Equation (5):

$$\left(\bar{\rho}\tilde{e}\right)_{,t} + \left(\bar{\rho}\tilde{u}_i\tilde{e}\right)_{,i} = \left(\left(\tilde{\kappa} + \kappa_T\right)\tilde{e}_{,i}\right)_{,i} + \overline{ps_{kk}} + \left(2\bar{\mu}\widetilde{s_{ij}s_{ij}} - \frac{2}{3}\bar{\mu}\widetilde{s_{kk}s_{ii}}\right) + \overline{Q} + S_T^e \tag{24}$$

where the extra source term originated from the unresolved turbulent heat fluxes is

$$S_T^e = \left[\kappa_T \frac{k}{\varepsilon}\left(c_1\tilde{s}_{ij} + c_2\tilde{\omega}_{ij}\right)\tilde{e}_{,j}\right]_{,i} \tag{25}$$

So far, this source term has not been considered in most of the RANS and LES simulations. Furthermore, equations similar to Equations (23) to (25) can be applied to any filtered species equation.

2.3 Time-Averaging Turbulent Quantities

Since various filters can be used to define the resolved turbulent quantities, a practical yet somewhat overlooked question is how to conduct an apple-to-apple comparison between the calculated results and the experimental data of turbulent flows.

Most of the experimental data are the "mean" values of turbulent variables (e.g., velocity, temperature, pressure, etc.); they are either the pure time-averaged values (for incompressible flows) or the density-weighted time-averaged values, i.e., the Favre-averaged values (for compressible flows):

$$\langle \phi \rangle = \lim_{T\to\infty} \frac{1}{T} \int_{-T/2}^{T/2} \phi \, dt, \quad [\phi] = \lim_{T\to\infty} \frac{1}{\langle \rho \rangle T} \int_{-T/2}^{T/2} \rho\phi \, dt, \tag{26}$$

where ϕ represents an instantaneous turbulent quantity, it can be u_i, $u_i u_j$, or $u_i u_j u_k$, etc., T is the entire time domain. $\langle \phi \rangle$ is the pure time-averaged (Reynolds-averaging) quantity and $[\phi]$is the density-weighted time-averaged (Favre-averaging) quantity. This type of experimental data is actually based on the assumption that the measured turbulent flows are statistically steady, or at least approximately steady. Otherwise, the experimental data of "mean" values must be redefined via the ensemble average of many repeated independent realizations of the (nominally) same experiment, i.e.,

$$\{\phi\} = \lim_{M\to\infty} \frac{1}{M} \sum_{i=1}^{M} \phi^{(i)}, \quad \frac{\{\rho\phi\}}{\{\rho\}} = \lim_{M\to\infty} \frac{1}{\{\rho\} M} \sum_{i=1}^{M} (\rho\phi)^{(i)}, \tag{27}$$

where M is the total number of realizations and $\phi^{(i)}$ and $(\rho\phi)^{(i)}$ are the values from each independent realization. The symbol { }represents the ensemble average. For statistically steady turbulent flows, the time average and the ensemble average become identical, i.e.

$$\{\phi\} = \langle \phi \rangle, \quad \frac{\{\rho\phi\}}{\{\rho\}} = [\phi]. \tag{28}$$

In summary, the experimental "mean" values for the compressible flows are either the density-weighted time average $[\phi]$ or the density-weighted ensemble average $\{\rho\phi\}/\{\rho\}$, expressed by Equations (26) and (27), respectively.

Now, in PRNS/VLES, the temporally filtered values $\overline{\phi}$, $\tilde{\phi}$ of turbulent variables are directly calculated. As a result, this enables an apple-to-apple comparison between the PRNS/VLES data and the experimental data. In Reference 1, relations between the PRNS/VLES data and the experimental data have been established for the first order, second order and higher order correlations. Furthermore, the relations for the Reynolds stresses and the scalar fluxes (which are second order moments formed by the zero-mean, fluctuating components of the velocities and scalars) can also be derived. Here we just present these relations under the statistically steady condition:

$$[u_i] = \langle \overline{\rho} \tilde{u}_i \rangle / \langle \overline{\rho} \rangle, \quad [e] = \langle \overline{\rho} \tilde{e} \rangle / \langle \overline{\rho} \rangle \tag{29}$$

$$[u_i e] = \langle \overline{\rho} \widetilde{u_i e} \rangle / \langle \overline{\rho} \rangle, \quad [u_i u_j] = \langle \overline{\rho} \widetilde{u_i u_j} \rangle / \langle \overline{\rho} \rangle, \quad [u_i u_j u_k] = \langle \overline{\rho} \widetilde{u_i u_j u_k} \rangle / \langle \overline{\rho} \rangle, \cdots. \tag{30}$$

Equation (29) indicates that the experimentally measured mean velocity and mean scalar (the terms on the left hand side of the equation) can be compared directly with the post-processed PRNS/VLES data (the terms on the right hand side). Even though Equation (30) cannot be used for direct comparison due to the unclosed terms on the right hand side, they are useful for establishing the following relationships for the Reynolds stresses and the scalar fluxes:

$$R_{ij} = T_{ij} + \left\langle \tau_{ij} \right\rangle \Big/ \left\langle \overline{\rho} \right\rangle, \tag{31}$$

$$R_i = T_i + \left\langle q_i \right\rangle \Big/ \left\langle \overline{\rho} \right\rangle, \tag{32}$$

where,

$$R_{ij} \equiv \left\langle \rho \left(u_i - [u_i] \right) \left(u_j - [u_j] \right) \right\rangle \Big/ \left\langle \rho \right\rangle = [u_i u_j] - [u_i][u_j], \tag{33}$$

$$R_i \equiv \left\langle \rho \left(u_i - [u_i] \right) \left(e - [e] \right) \right\rangle \Big/ \left\langle \rho \right\rangle = [u_i e] - [u_i][e], \tag{34}$$

$$T_{ij} = \left\langle \overline{\rho} \tilde{u}_i \tilde{u}_j \right\rangle \Big/ \left\langle \overline{\rho} \right\rangle - \left\langle \overline{\rho} \tilde{u}_i \right\rangle \left\langle \overline{\rho} \tilde{u}_j \right\rangle \Big/ \left\langle \overline{\rho} \right\rangle^2, \tag{35}$$

$$T_i = \left\langle \overline{\rho} \tilde{u}_i \tilde{e} \right\rangle \Big/ \left\langle \overline{\rho} \right\rangle - \left\langle \overline{\rho} \tilde{u}_i \right\rangle \left\langle \overline{\rho} \tilde{e} \right\rangle \Big/ \left\langle \overline{\rho} \right\rangle^2 . \tag{36}$$

The experimentally measured Reynolds stresses R_{ij} and the scalar fluxes R_i are determined according to Equations (33) and (34), respectively. Their PRNS/VLES counterparts, on the right hand side of Equations (31) and (32), consist of two components: the first component, T_{ij} or T_i, can be determined by using the resolved variables according to Equation (35) or (36); the second component, the unresolved turbulence stresses τ_{ij} or the scalar fluxes q_i, will have to be obtained via the subscale models, Equations (8) and (23), discussed in the previous section. It is not difficult to recognize that the second component will evolve to the total Reynolds stresses and fluxes when the width of the temporal filter becomes sufficiently large, i.e., the contributions from both T_{ij} and T_i should vanish.

2.4 Guideline for Conducting the Simulation

In the unfiltered turbulent flow field, the smallest time, length and velocity scales are the Kolmogorov micro-scales (Ref. 15). By invoking an analogy to the Kolmogorov micro-scales, the smallest time, length and velocity scales occurring in the filtered field are

$$\tau_{prns} = \left(\frac{\overline{\nu}_T + \nu}{\overline{\varepsilon}} \right)^{\frac{1}{2}}, \quad \eta_{prns} = \left(\frac{\left(\overline{\nu}_T + \nu \right)^3}{\overline{\varepsilon}} \right)^{\frac{1}{4}}, \quad \upsilon_{prns} = \left[\left(\overline{\nu}_T + \nu \right) \overline{\varepsilon} \right]^{\frac{1}{4}} \tag{37}$$

Equation (37) indicates that, in addition to the viscosity of the fluid ν, these smallest scales also depend on the mean values of subscale eddy viscosity $\overline{\nu}_T$ and dissipation rate $\overline{\varepsilon}$, which are turbulent flow properties. Following Equation (37), the relationship between the length scale η_{prns} and the time scale τ_{prns} is

$$\eta_{prns} = \left[\tau_{prns} \left(\overline{\nu}_T + \nu \right) \right]^{\frac{1}{2}} \tag{38}$$

Equation (38) indicates that for a fixed smallest time scale τ_{prns} (its minimum value should be Δ_T in the filtered field), the smallest length scale η_{prns} can automatically adjust itself to the change of the mean subscale eddy viscosity $\overline{\nu}_T$, or vice versa, i.e. the mean subscale eddy viscosity $\overline{\nu}_T$ will adjust itself to the given local grid spacing which, in this scenario, is viewed as the local smallest length scale η_{prns}. In this sense, there is some leeway in selecting the grid spacing for a given temporal filter width. Equation (38) also suggests that, for a given Δ_T, when $\overline{\nu}_T$ is no longer changing with respect to the reduction of grid spacing, the smallest length scale in the temporally filtered field will also not be affected by grid spacing reduction, i.e., a grid independent solution is reached.

At the governing equation level, $\overline{\nu}_T$ and $\overline{\varepsilon}$ are functions of the resolution control parameter RCP (i.e., the temporal filter width). At the numerical solution level, their calculated values are functions of the RCP as well as the local grid spacing. The consistency conditions require that the resulted time scale τ_{prns} is of the same order of the temporal filter width Δ_T, and the resulted length scale η_{prns} can be of the same order of the grid spacing or larger. In practice, these two conditions can only be rigorously verified posterior, because the values of the time and length scales (τ_{prns}, η_{prns}) will not be known until the simulation is completed. As a rule of thumb, a 'successful' simulation often is indicative of these two conditions being by and large satisfied.

2.4.1 Resolution Control Parameter RCP

The resolution control parameter *RCP* (i.e., the ratio Δ_T/T) is used in PRNS/VLES to regulate the content of the time scales of the resolved turbulence. When $RCP \rightarrow 1.0$, all time scales of turbulence have been filtered (i.e., modeled), and the PRNS/VLES simulation becomes a RANS simulation, i.e., the directly calculated field is intrinsically the time mean, no turbulent fluctuation occurs in the directly calculated quantities. As the value of *RCP* decreases, the turbulent fluctuation becomes more pronounced in the directly calculated field, and the simulation moves towards VLES or LES.

To carry out a very large eddy simulation, we need to choose a value of *RCP* from the outset. The consistency condition requires that τ_{prns} is of the same order of the temporal filter width Δ_T. Therefore, by using Equation (37), we have

$$\Delta_T = \left(\frac{\overline{\nu}_T + \nu}{\overline{\varepsilon}} \right)^{\frac{1}{2}} \approx \frac{\overline{k}}{\overline{\varepsilon}} \tag{39}$$

This is based on the assumption that $\overline{\nu}_T \gg \nu$ for a very large eddy simulation and the mean subscale eddy viscosity $\overline{\nu}_T$ is of the order of $\overline{k}^2/\overline{\varepsilon}$, where $\overline{k}$ and $\overline{\varepsilon}$ are the mean value of subscale kinetic energy and its dissipation rate. As a result, the resolution control parameter *RCP* (Δ_T/T) is estimated according to

$$RCP = \frac{\Delta_T}{T} \sim \frac{\overline{k}/\overline{\varepsilon}}{k_{ref}/\varepsilon_{ref}} \sim \frac{\overline{k}}{k_{ref}} \tag{40}$$

where T is the global time scale of interested turbulent flow and is expressed as a ratio of the reference turbulent kinetic energy to its dissipation rate. We have also assumed that ε_{ref} and $\overline{\varepsilon}$ are of the same order, since the dissipation mostly concentrates in the small scales (Ref. 15). Equation (40) suggests a way to guide the selection of the value of *RCP*. For example, *RCP* = 0.20 means that we intend to directly resolve those turbulence scales that are responsible for about 80 percent of the total turbulent kinetic energy while to model the rest unresolved turbulence scales that contain about 20 percent of the total turbulent kinetic energy.

In the simulations presented in Section 3.0, the coefficient $f(\Delta_T/T)$ for the subscale model in Eq. (8) is set to be 0.3, 0.3333 and 0.4444 for the pipe flow, the LM6000 injector and the LDI combustor, respectively. According to Equation (14), the respective Δ_T/T is about 0.16, 0.18 and 0.25, which means

that the PRNS/VLES simulation is to resolve the large scale turbulence that contains about 84 percent of the total turbulent kinetic energy for the pipe flow, 82 percent for the LM6000 injector and 75 percent for the LDI combustor.

2.4.2 Arrangement of Numerical Grid Spacing and Grid Independent Solution

Usually, a computational grid based on a priori knowledge of the flow field is generated subject to the constraint of the available computing resources. Typically, finer grid spacing is used in regions where the shear rates are higher and the turbulent fluctuations are stronger. Then we decide, as practically as possible, the extent to which the turbulence is to be resolved at the governing equation level and choose a value of *RCP* according to Equation (40). As discussed above, the consistency of the calculated results needs to be assessed posterior. In general, simulations with different levels of coarse grid spacing are all legitimate as long as the consistency conditions are satisfied. And of course, finer grid spacing is capable of revealing finer turbulent structures, but the statistical mean should be about the same. By refining the grid, it is possible to attain a grid independent solution; the criterion should be that for a given value of RCP the calculated mean values of τ_{prns} and η_{prns} do not change when the grid spacing is further reduced.

3.0 Numerical Results of PRNS/VLES Simulations

The simulations of three internal flows will be presented, the first one is a turbulent pipe flow to illustrate the basic features of PRNS/VLES; the second one is a swirling turbulent flow associated with a GE LM6000 single injector to further demonstrate the advantage of the nonlinear model over the pure eddy viscosity model; and the third one is the flow in a single-element lean direct injection combustor. The last simulation was performed with a relatively coarse grid but for a quite complex geometry, and the dynamically important, unsteady turbulent flow structures have been revealed.

3.1 Pipe Flows

The turbulent pipe flow is one of the ideal benchmark flows for evaluating/validating numerical simulation approaches, because the geometry is simple and the flow is statistically homogeneous in the axial direction so that periodic boundary conditions can be applied to the inlet and the outlet to avoid the often complicated boundary-condition issues. In addition, some experimental data (Ref. 16) are available for comparison.

Turbulent pipe flows at several different Reynolds numbers (from high to low) have been used to evaluate the fundamentals of the PRNS/VLES approach (Ref. 17). At each Reynolds number, the simulation was performed over a range of *f (RCP)* (from 0.2 to 1.0) to demonstrate the unified feature of the current approach. Also, two types of subscale models were used for flow simulation at each Reynolds number: one is a pure eddy viscosity model, and the other is a nonlinear model described by Equation (8). We have noticed that the nonlinear subscale model is critically important for the successful simulation of low Reynolds number pipe flow. Here we present some of the results at two Reynolds numbers: $Re_\tau = 180$ and 3322 (based on the pipe radius and friction velocity). The value of *f (RCP)* was set to 0.3, which is a typical value for a very large eddy simulation.

The computational domain has an aspect ratio of Length/Radius = 10, where Radius = 0.06468 m. Figure 1 shows the grid spacing in a cross section of the pipe. The grid is nearly orthogonal everywhere. The total number of the hexahedral elements is 906,750, more specifically, $(156 \times 29 + 39 \times 39) \times 150$.

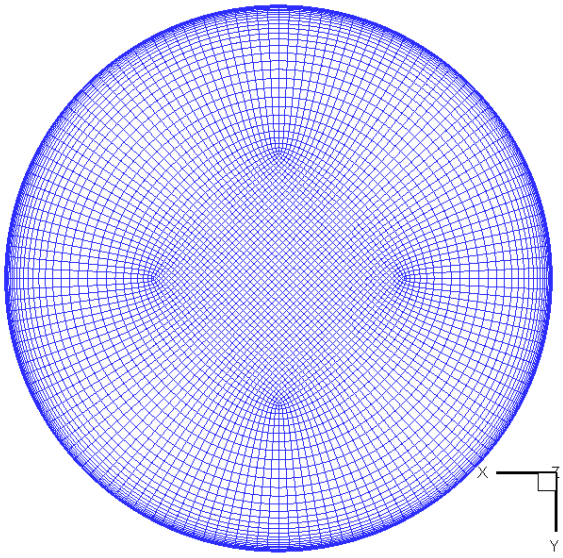

Figure 1.—Grid spacing in a cross section of the pipe.

This grid was used for flows at both Reynolds numbers 180 and 3322. The initial flow field was created by an arbitrary smooth profile plus random fluctuations. At the wall, a generalized wall function was imposed (Ref. 18).

3.1.1 Reynolds Number Re τ= 180

Turbulent pipe flow at the low Reynolds number Re τ = 180 (or Re = 7,000 based on the pipe diameter and centerline velocity) is relatively weak. In this section, we will present the numerical results, which demonstrate that for such a low Reynolds number turbulent flow, the pure eddy viscosity subscale model is unable to develop and sustain turbulent fluctuations in the numerical simulation.

3.1.1.1 Nonlinear Subscale Model

The PRNS/VLES simulation using the nonlinear subscale model given by Equation (8) has successfully simulated the turbulent pipe flow. The transition from the initial disturbances to the fully developed, large scale turbulence can clearly be identified from the time histories of the velocity components (w, u and v). For a fully developed turbulent pipe flow, the turbulent fluctuations are stronger near the wall where the shear rates are higher. Near the centerline, the turbulent fluctuations are weaker. We have arranged 15 probes along a radius of the pipe to record the time history of the flow variables. Also, we have another 16 probes along the centerline to examine the statistical homogeneity in the axial direction. Here we only present the time histories of three velocity components at the probe 1, which is located at the center of the pipe.

The time history of the velocity indicates that the initially induced random fluctuations are significantly damped during the first 600 time steps, then fluctuations quickly grow and evolve into a fully developed turbulence (See Figs. 2 and 3).

The instantaneous contours of the axial velocity in a center plane (Fig. 4) and in a cross section (Fig. 5) clearly demonstrate the motions of various turbulent scales.

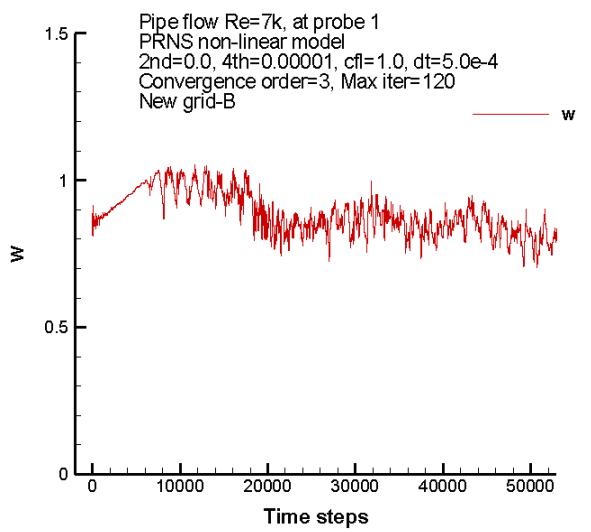

Figure 2.—Time history of the axial velocity.

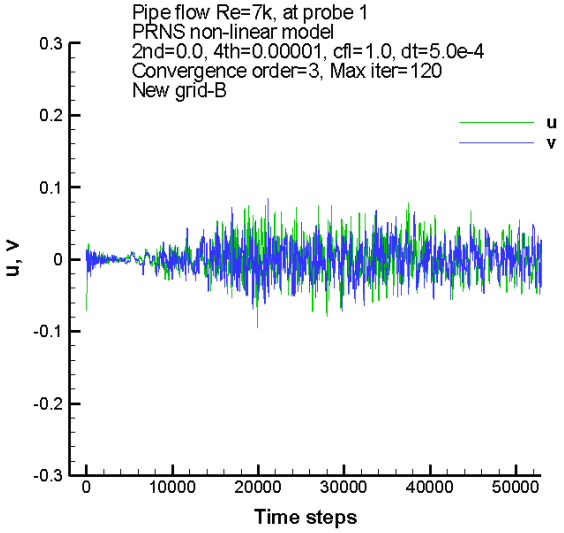

Figure 3.—Time history of the u, v components.

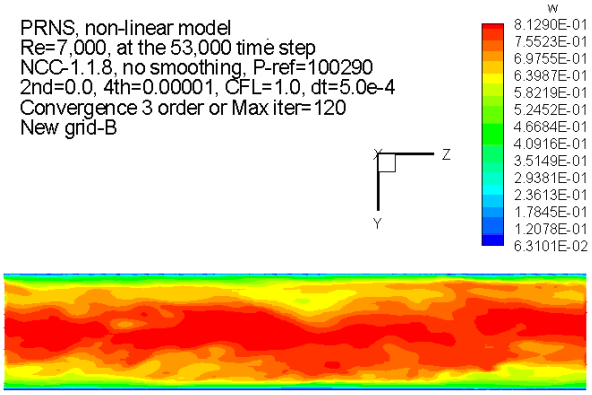

Figure 4.—Contour of axial velocity in a center plane.

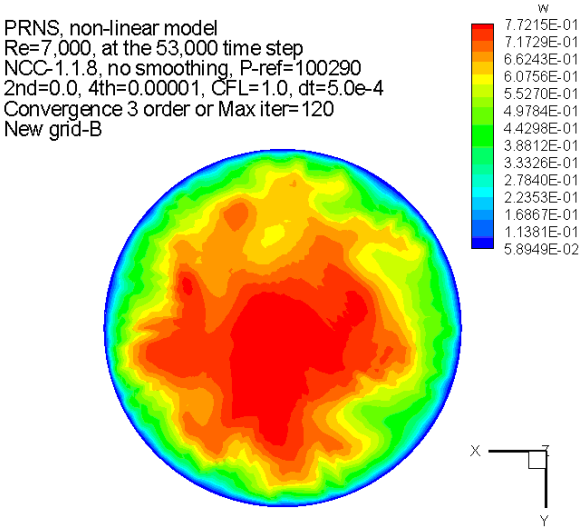

Figure 5.—Contour of axial velocity in a cross section.

3.1.1.2 Linear Subscale Model

The PRNS/VLES simulation using the pure eddy viscosity subscale model is unable to develop the turbulent fluctuation into a fully developed turbulent pipe flow. The time histories of the three velocity components w, u and v at the center of the pipe indicate that the initially induced random fluctuations are quickly damped out and no new turbulent fluctuation emerges (see Figs. 6 and 7).

Figures 8 and 9 are the contours of the axial velocity in a center plane and in a cross section of the pipe. These smooth contours do not show any turbulent fluctuating feature.

To further study these phenomena, we have restarted a simulation using the eddy viscosity subscale model but starting from a fully developed turbulent flow field obtained in Section 3.1.1.1. We have observed that this initial fully developed turbulence could not be sustained, in fact, it was quickly annihilated. Then we continued the simulation by turning on the nonlinear subscale model, and we found that the turbulent fluctuations quickly re-emerged and evolved into a fully developed turbulent pipe flow. The results of above simulations suggest that the pure eddy viscosity model is not suitable for PRNS/VLES simulation of relatively weak turbulent flow which has a low Reynolds number.

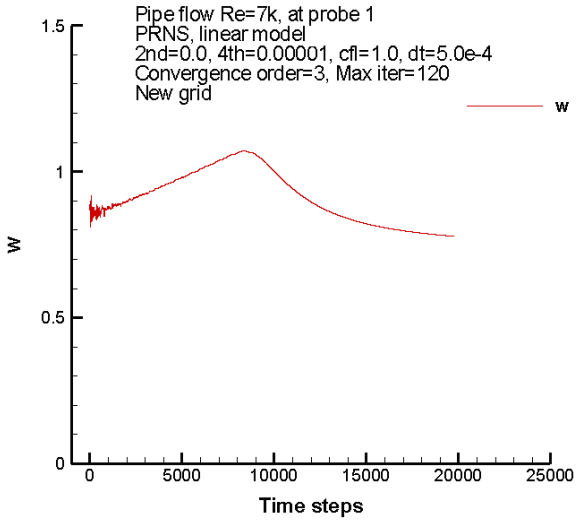

Figure 6.—Time history of the axial velocity w.

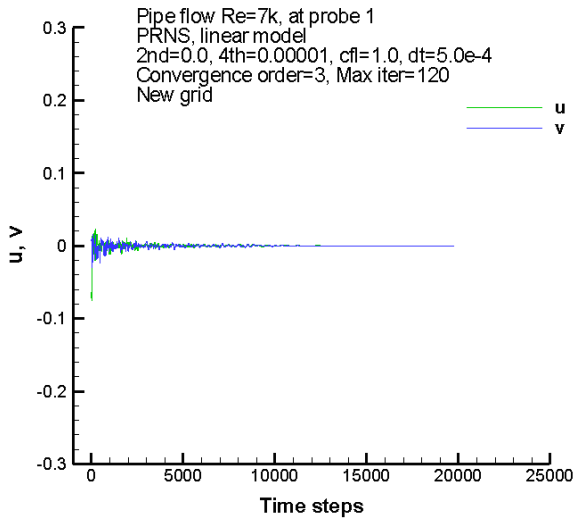

Figure 7.—Time history of the velocity components u, v.

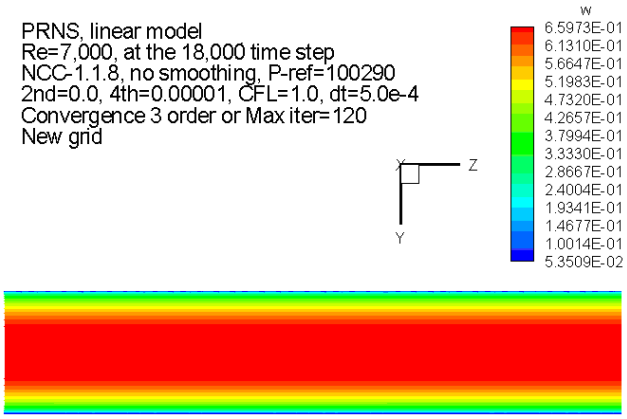

Figure 8.—Contour of w component in a center plane.

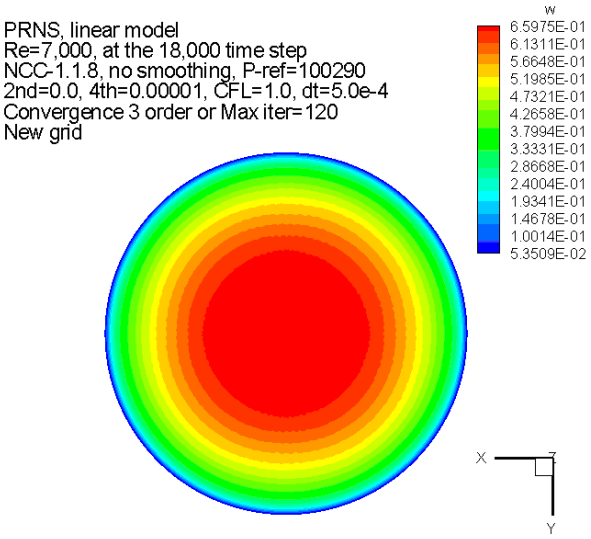

Figure 9.—Contour of w component in a cross section.

3.1.2 Reynolds Number Re τ = 3322

Turbulent pipe flow at high Reynolds number Re τ= 3322 (or Re = 150,000 based on the pipe diameter and centerline velocity) has quite strong turbulence. These strong turbulent fluctuations are easy to sustain in the numerical simulation, even with the use of pure eddy viscosity subscale model. We have performed simulations using *f (RCP)* = 0.3 with both the nonlinear subscale model and the linear eddy viscosity model. In both cases, the initially induced random fluctuations were able to evolve into the fully developed turbulent fluctuations. Here we only present the numerical results from using the nonlinear subscale model.

3.1.2.1 Time History

The time histories of the velocity components w, u, v and the subscale turbulent kinetic energy are recorded at 15 probes along a radius in a cross section at the mid-length of the pipe. Figures 10 to 15 present the time histories of the axial velocity and the subscale turbulent kinetic energy *k* at the probes 1, 6, and 14, which correspond to the locations r/R = 0.0, 0.5, and 0.9743, or y^+ = 3322, 1661 and 85.

Probe 1 is at the center of the pipe, Probe 6 is at the midpoint between the center and the pipe wall, and Probe 14 is very close to the wall. The time histories at other 28 locations along the pipe radius and axis are also available. These time histories indicate that the initially induced disturbances of the velocity components are at first somewhat damped, followed by the emergence of new fluctuations, which are then quickly amplified and evolved into a fully developed turbulent pipe flow. The amplitude of the velocity fluctuations increases from the center towards the wall, so does the unresolved turbulent kinetic energy.

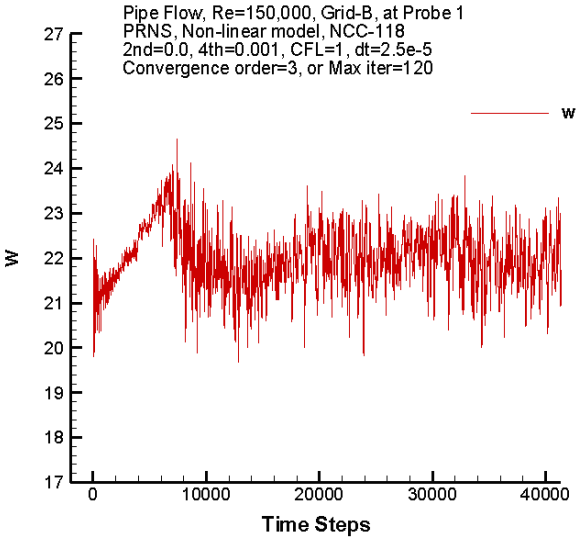

Figure 10—Time history of w component at Probe 1.

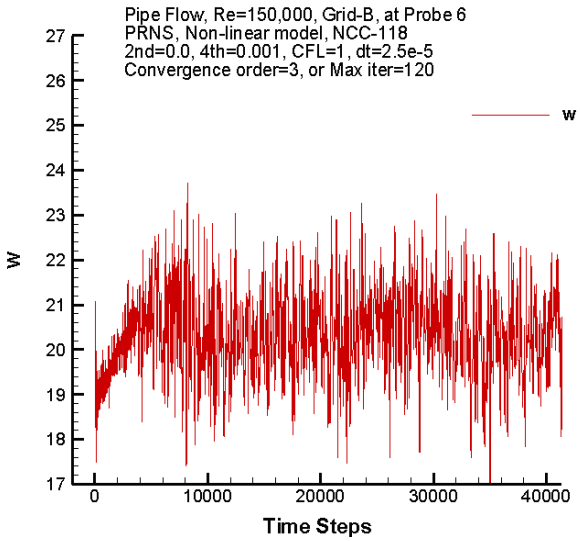

Figure 11—Time history of w component at Probe 6.

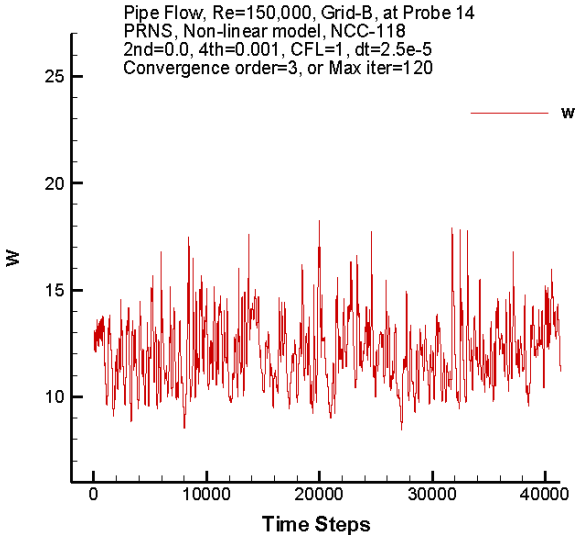

Figure 12—Time history of w component at Probe 14.

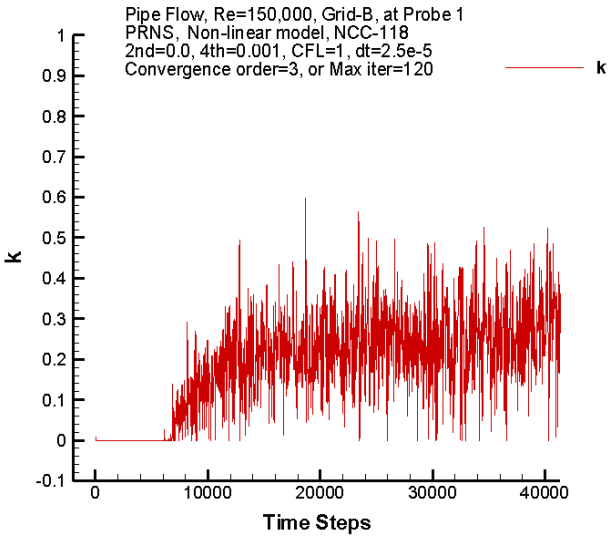

Figure 13.—Time history of k at Probe 1.

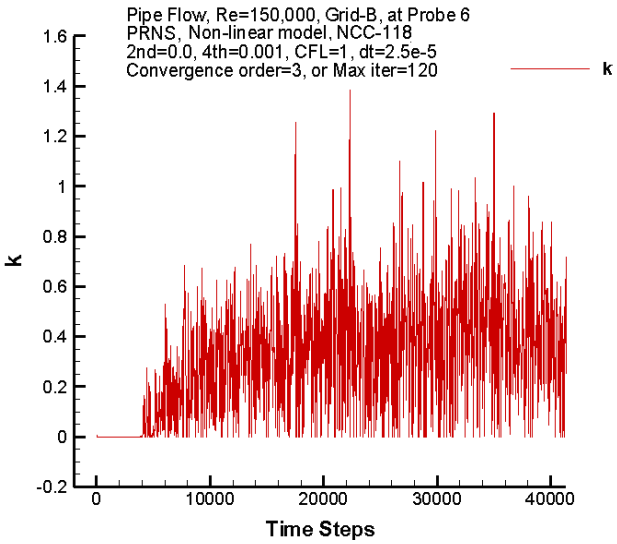

Figure 14.—Time history of k at Probe 6.

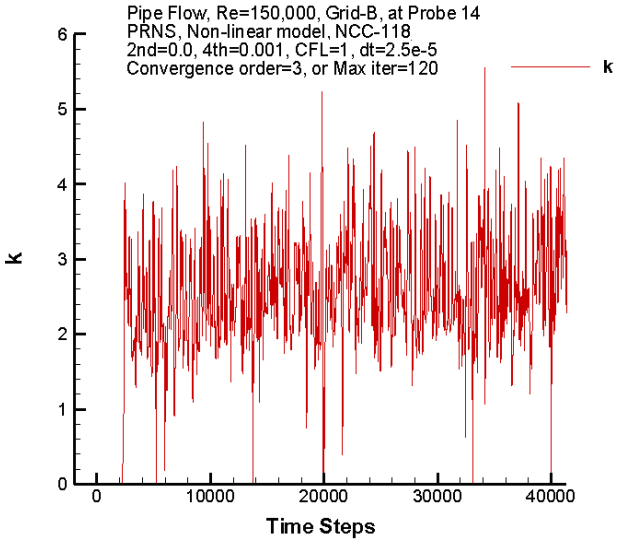

Figure 15.—Time history of k at Probe 14.

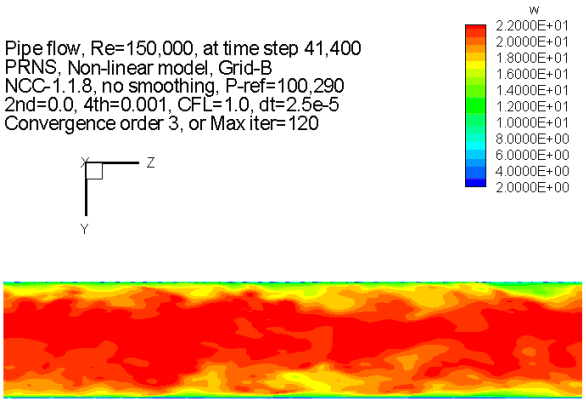

Figure 16.—Contour of w component in a center plane.

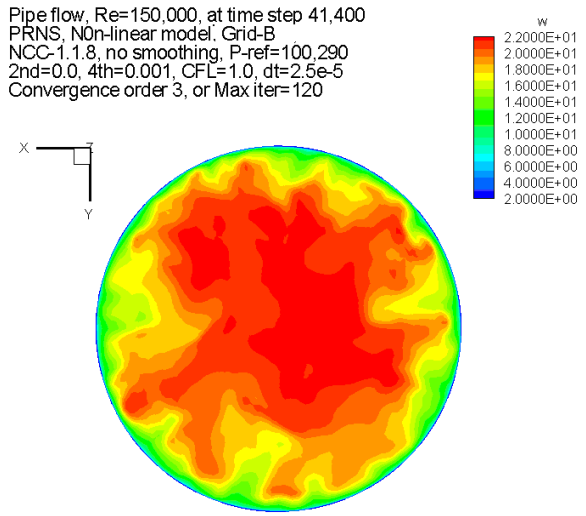

Figure 17.—Contour of w component in a cross section.

3.1.2.2 Instantaneous Contour

To examine the turbulent flow structures, we have plotted the instantaneous contours of various variables in a center plane and in a cross section. Here we present the instantaneous contours of the axial velocity component, the vorticity magnitude, the subscale turbulent kinetic energy and the effective subscale viscosity in Figures 16 to 23. The contours of the velocity component and the vorticity magnitude illustrate the features of the resolved large scale turbulent structures, whereas the subscale turbulent kinetic energy and the effective viscosity illustrate the highly non-uniform features of the unresolved scales.

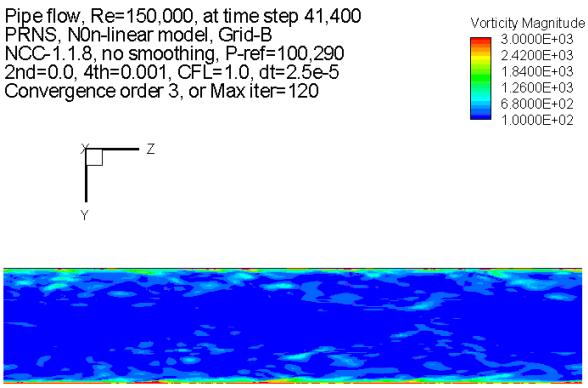

Figure 18.—Contour of the vorticity in a center plane.

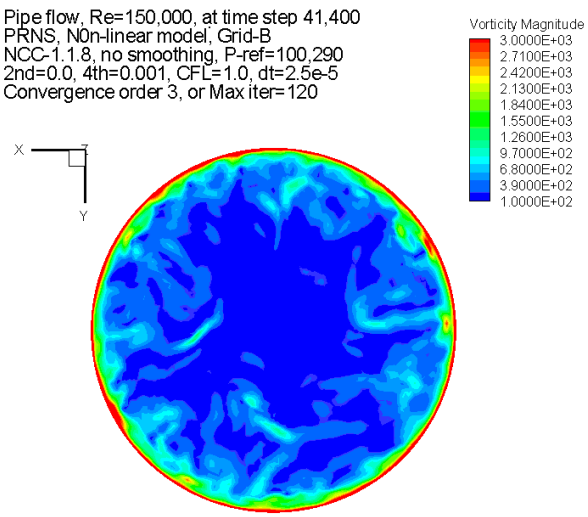

Figure 19.—Contour of the vorticity in a cross section.

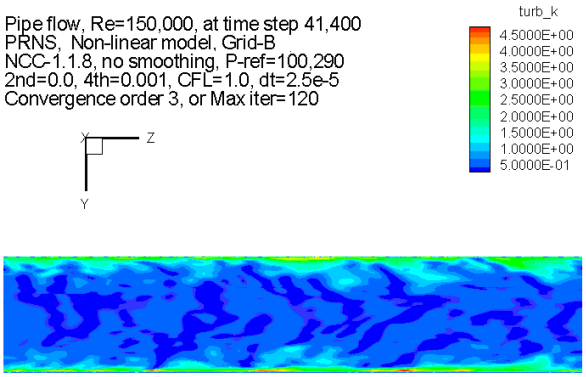

Figure 20.—Contour of k in a center plane.

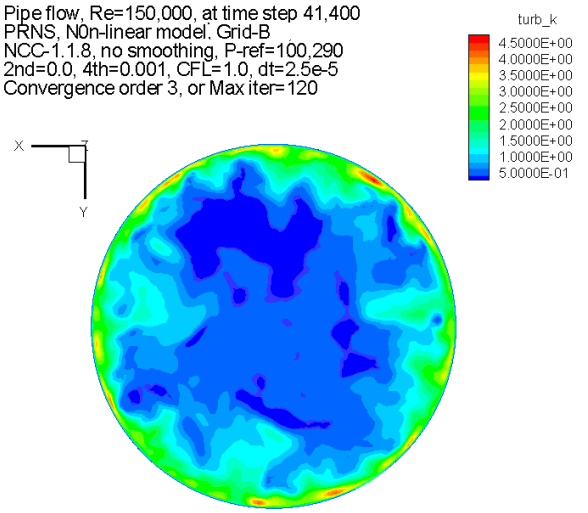

Figure 21.—Contour of k in a cross section.

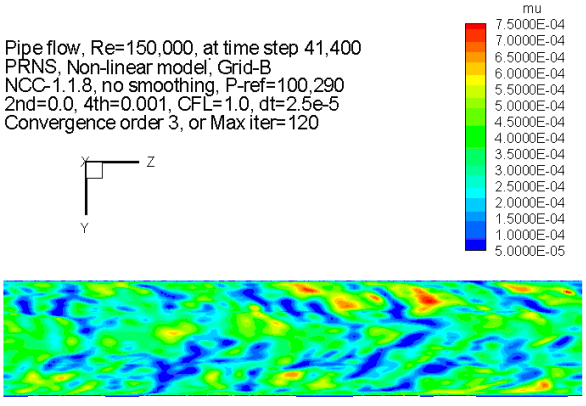

Figure 22.—Contour of effective viscosity in a center plane.

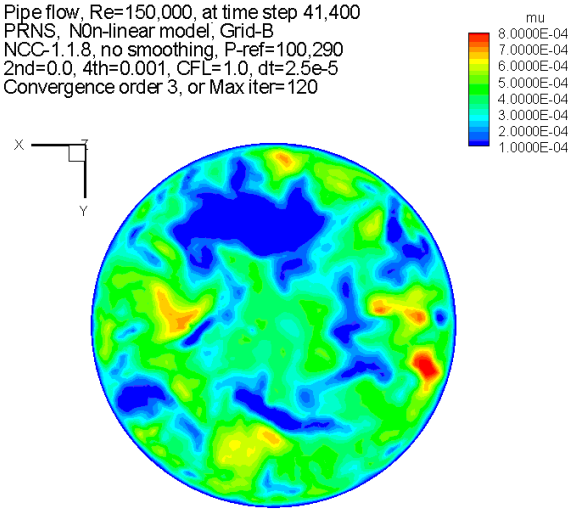

Figure 23.—Effective viscosity in a cross section.

3.1.2.3 Radial Profile

The radial profiles of various flow variables (w, u, v, gauge pressure, vorticity magnitude, Mach number, subscale turbulent kinetic energy and dissipation rate, effective subscale eddy viscosity) are examined at different locations along the pipe axis z = 0.0, 0.1, 0.2, 0.3, 0.4, 0.5, 0.6, 0.645 for the spatial development of the turbulent flow. Note that z is non-dimensionalized with the pipe radius. Figure 24 shows the experimentally measured mean axial velocity (Ref. 16) together with the (calculated) instantaneous axial velocity at six downstream locations. Figure 25 presents the profiles diametrically. Figures 26 and 27 illustrate the radial profiles of the subscale turbulent kinetic energy and the effective viscosity, respectively. These results indicate that the simulated turbulent flow is fully developed and is statistically homogeneous along the pipe.

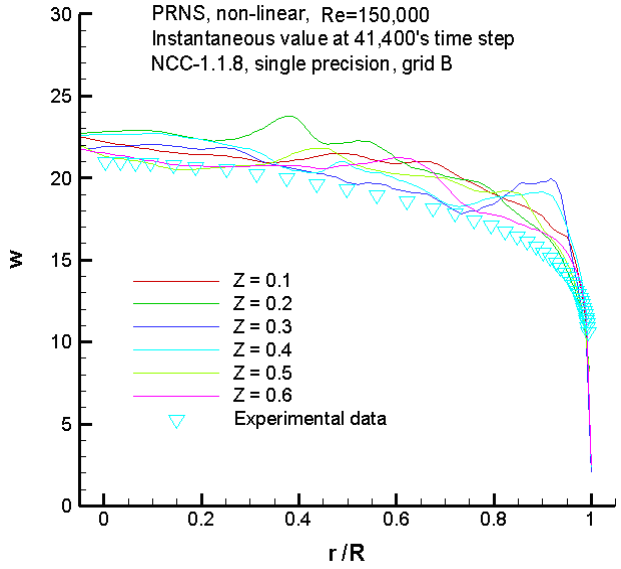

Figure 24.—Radial profile of the axial velocity.

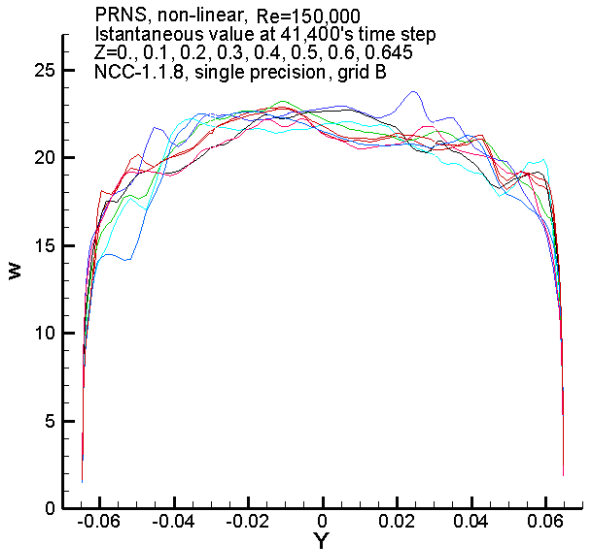

Figure 25.—Radial profile of instantaneous axial velocity.

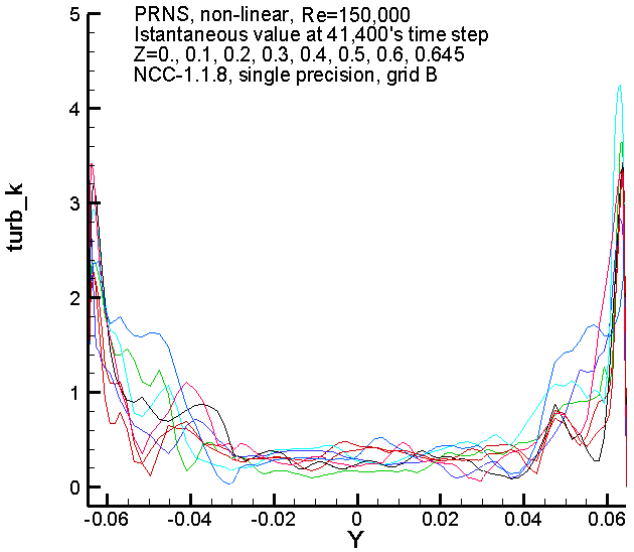

Figure 26.—Radial profile of instantaneous k.

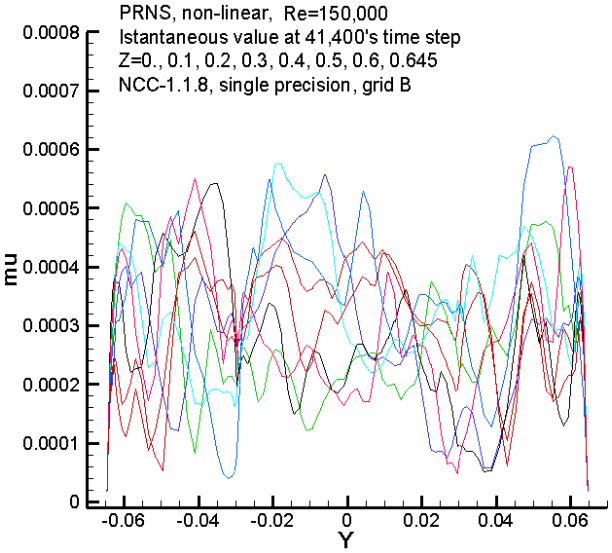

Figure 27.—Radial profile of instantaneous effective viscosity.

3.1.2.4 Spectrum and Correlation Analysis

Figure 28 and 29 present the power spectrum density (PSD) of the axial velocity component and its two-point (time) correlation at three locations (Probes 1, 6 and 14). The broadband feature of the PSD (i.e., more than two orders of energy variation from small scale to large scale) and the typical two-point correlation shapes (i.e., the correlation rapidly decreases as the time lag increases) indicate that the PRNS/VLES simulation with $f\,(RCP) = 0.3$ does mimic the statistical features of a fully developed turbulence.

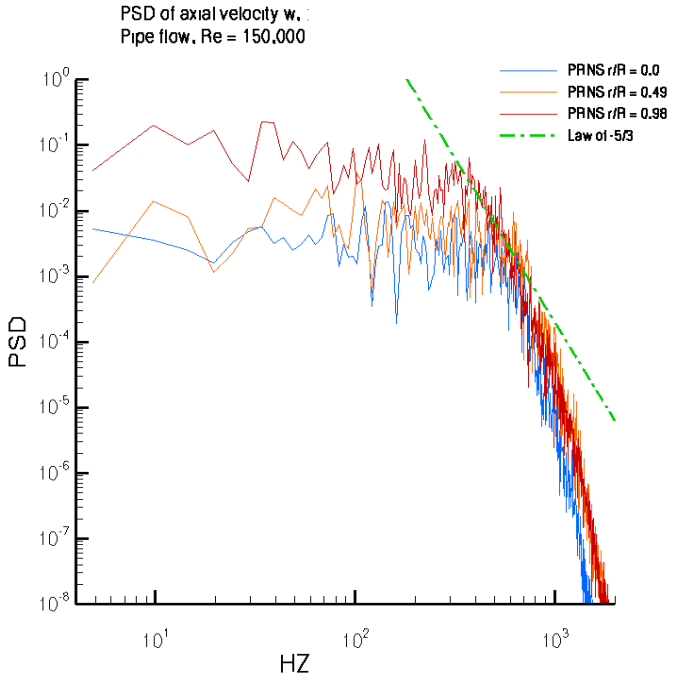

Figure 28.—Power spectrum density of the axial velocity at Probes 1, 6 and 14.

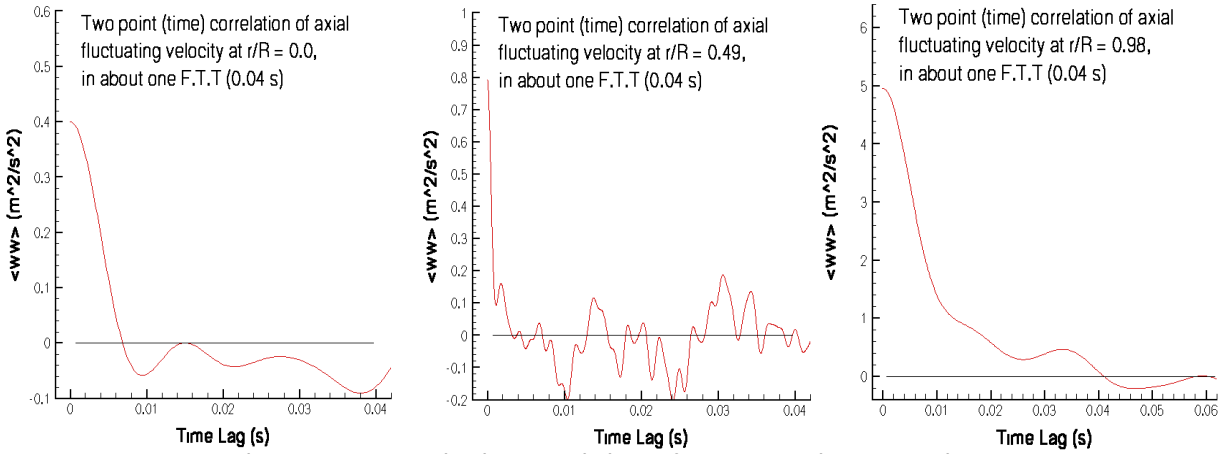

Figure 29.—Two-point time correlations of <ww> at Probes 1, 6 and 14.

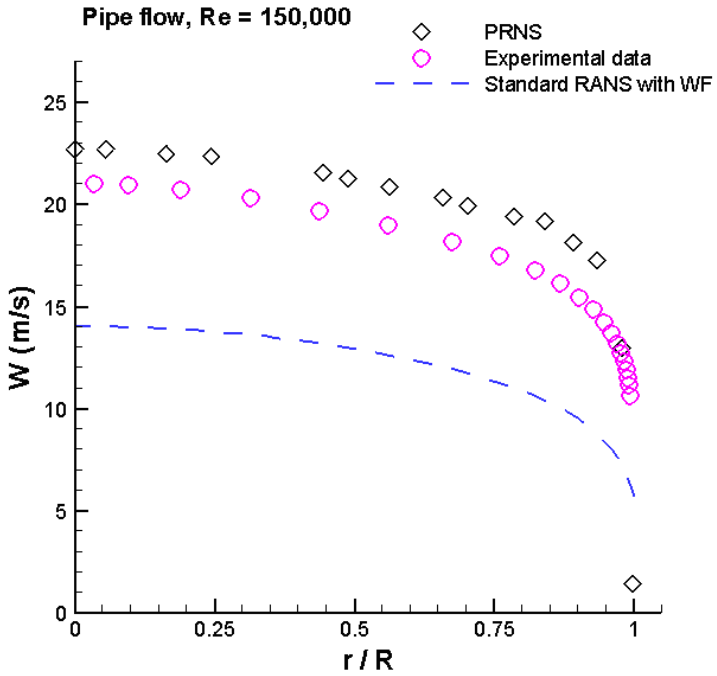

Figure 30.—Comparison of mean axial velocity between PRNS/VLES, URANS and experimental data.

The experimental data of the mean axial velocity at Reynolds number of 145,700 is used to compare the time averaged axial velocity obtained from the current simulation at a Reynolds number of 150,000. In Figure 30, the result obtained from URANS using a standard $k-\varepsilon$ model and the wall function is included. The result obtained from PRNS/VLES is in reasonable agreement with the experimental data, while the URANS result exhibits significant under-prediction.

3.2 Flow in a Single-Element LM6000 Injector

LM6000 is a General Electric low NOx gas turbine. We have performed several types of numerical simulation of the flow issued from one of its fuel injector. A highly swirling jet is injected from a circular inlet. The inlet pressure is about six atmospheres and the inlet temperature is about 644 K. The inlet boundary condition is the specified mean profiles from the experiments. The combustor is a rectangular box. The Reynolds number based on the inlet axial velocity and the inlet jet diameter is about 3,200,000. Figure 31 depicts the computational domain and the numerical grid. The total number of the grid points is about 495,000. This is the only grid used in this study to perform all of the simulations including PRNS/VLES, URANS and RANS. Here we only present the results from the very large eddy simulation using the PRNS/VLES approach.

The value of *f (RCP)* is set to 0.3333. A convective unsteady boundary condition (Ref. 19), similar to that proposed by Ferziger (Ref. 20) and Grinstein, et al (Ref. 21), is applied at the outlet boundary. The initial condition is the solution of a steady RANS simulation (see Figs. 32 and 33 for the axial velocity u and the vorticity magnitude in a center plane). Two subscale models (nonlinear and linear) have been used. The results indicate that the nonlinear model is very helpful in the simulation of swirling turbulent flow, which occurs commonly in the combustor system.

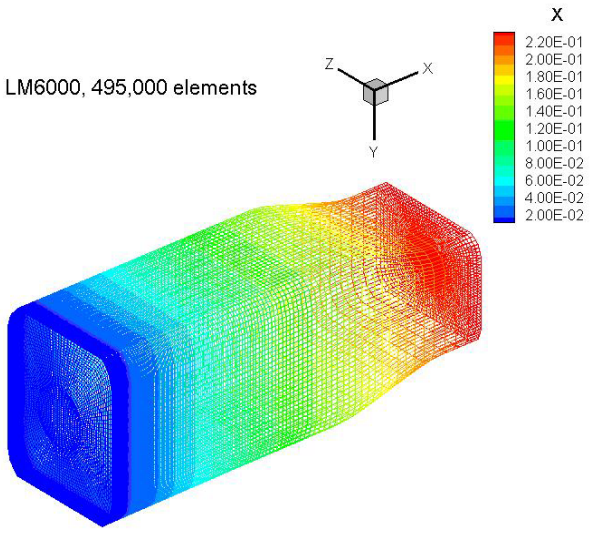

Figure 31.—Computational domain for LM6000 single injector flow simulation.

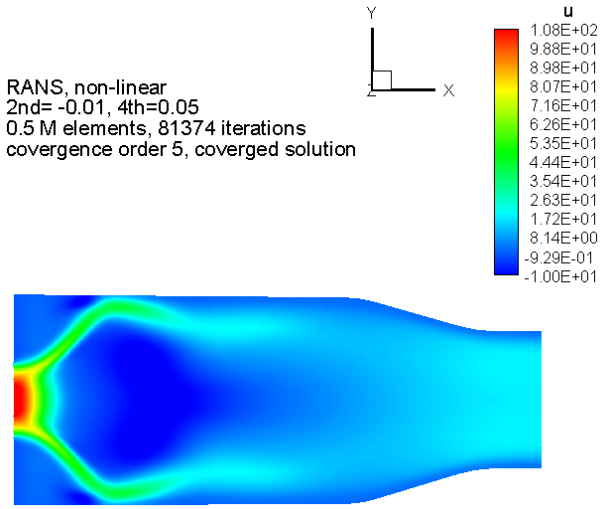

Figure 32.—Contour of the axial velocity (RANS).

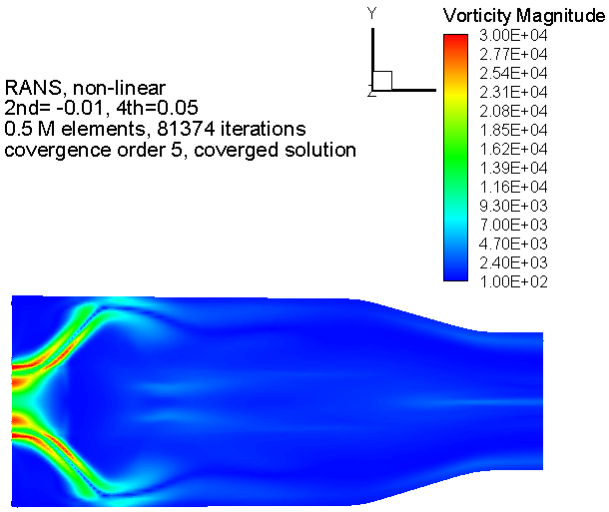

Figure 33.—Contour of the vorticity magnitude (RANS).

3.2.1 Nonlinear Subscale Model

The time history of velocity components and gauge pressure are recorded at four locations along the centerline: x = 0.015, 0.05, 0.10 and 0.2 m. From which we may monitor the development of turbulent fluctuations. Here, the presented time histories of the velocity components are at x = 0.1 and 0.2 m, which are located before and after the rear stagnation point of the recirculation zone. Figures 34 and 35 indicate that the turbulent fluctuations are fully developed.

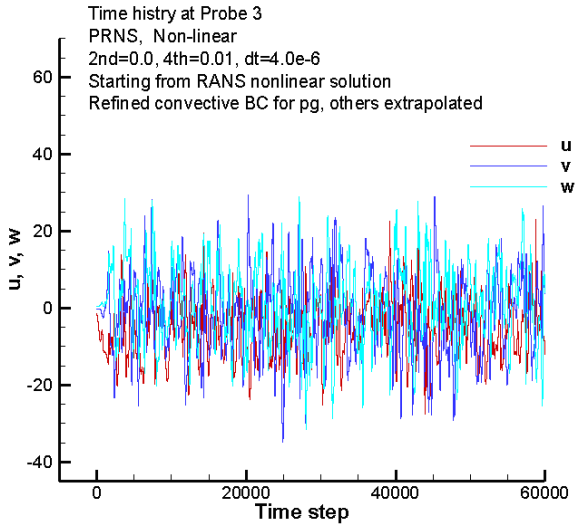

Figure 34.—Time histories of velocity at Probe 3.

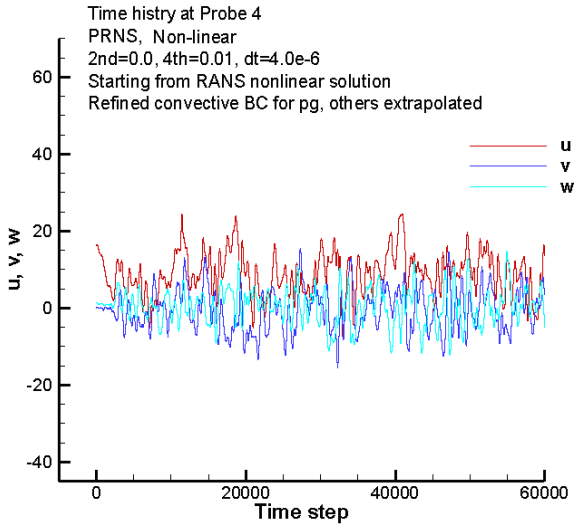

Figure 35.—Time histories of velocity at Probe 4.

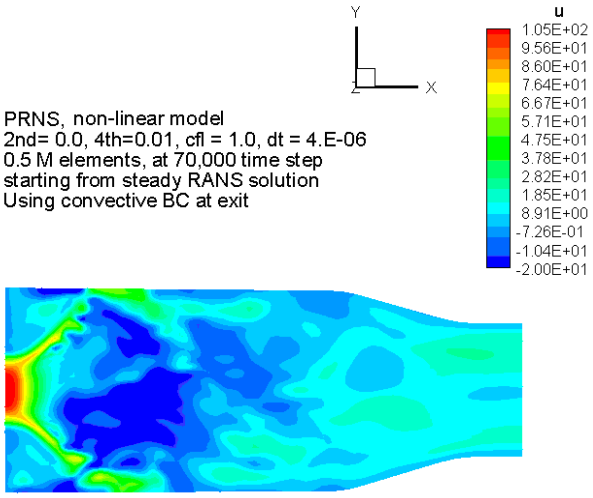

Figure 36.—Contour of instantaneous axial velocity.

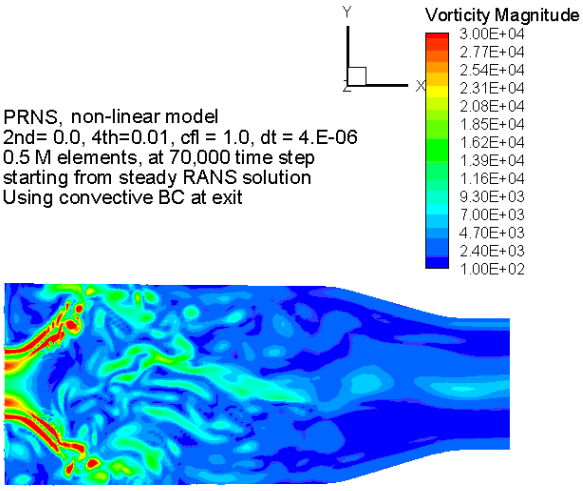

Figure 37.—Contour of instantaneous vorticity.

The instantaneous contours of flow variables in a center plane are presented for the time step 60,000 which is about 100 through flow times (TFT, defined as the ratio of the length of the combustor to the inlet centerline axial velocity). Figures 36 and 37 are the contours of the axial velocity and the vorticity magnitude, respectively. The recirculation zone, the massive separation and the shear layers are clearly visualized.

3.2.2 Linear Subscale Model

In the early stage of the simulation, the calculated turbulent structures look reasonable. However, they are not sustainable in the long run, and the calculation crashes after 18,000 time steps (about 36 times of the through flow time, TFT).

Here, we present the instantaneous contours at two instances: the time step 10,000 (about 20 TFT) and the time step 18,000 (about 36 TFT). Around 20 TFT, the flow structures, shown in Figures 38, 40

and 42, look reasonable except for the subscale turbulent quantities. The subscale turbulent kinetic energy k (not shown) and the eddy viscosity μ_T are too small (about two orders of magnitude smaller) when compared with its counterpart obtained from the nonlinear subscale model. Around 36 TFT, the flow structure near the outlet becomes unphysical (see Figs. 39, 41 and 43), e.g., large amount of high speed inflow occur at the exit. The subscale turbulent kinetic energy (not shown) and the eddy viscosity become even weaker and smaller. The simulation crashes soon after 36 TFT. These results suggest that the linear subscale $k-\varepsilon$ model does not work very well for highly swirling flows.

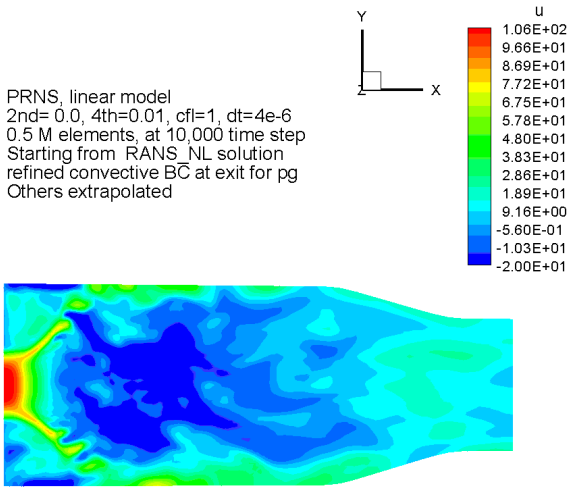

Figure 38.—Axial velocity at 10,000 time step.

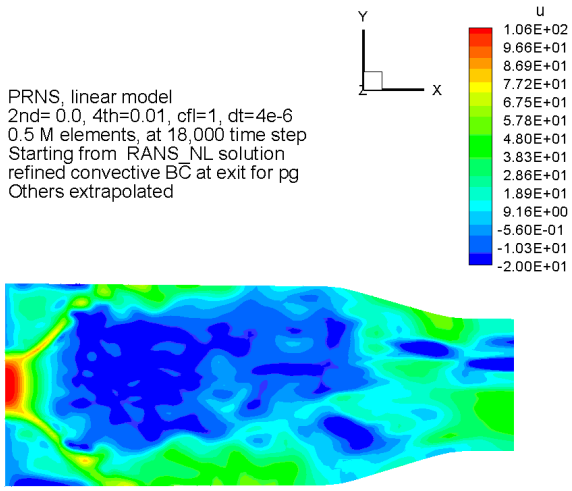

Figure 39.—Axial velocity at 18,000 time step.

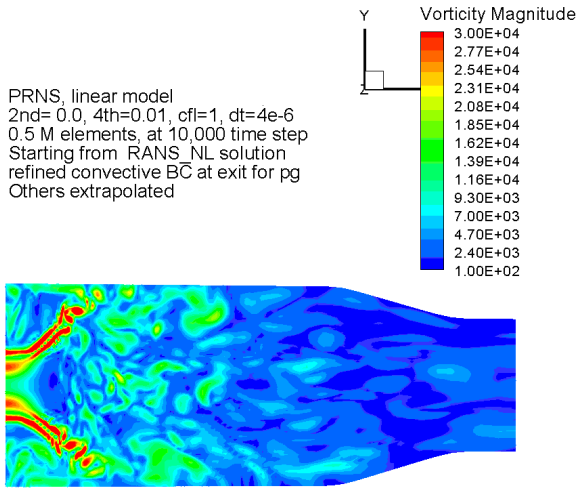

Figure 40.—Contour of vorticity at 10,000 time step.

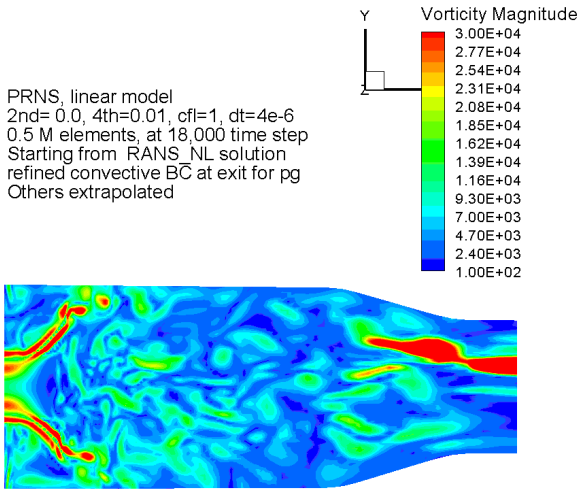

Figure 41.—Contour of vorticity at 18,000 time step.

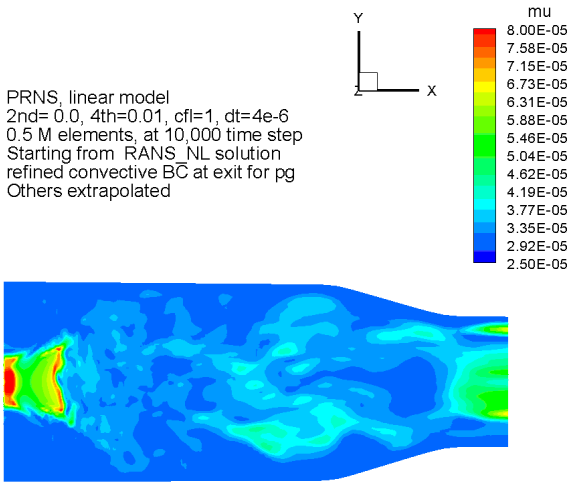

Figure 42.—Effective viscosity at 10,000 time step.

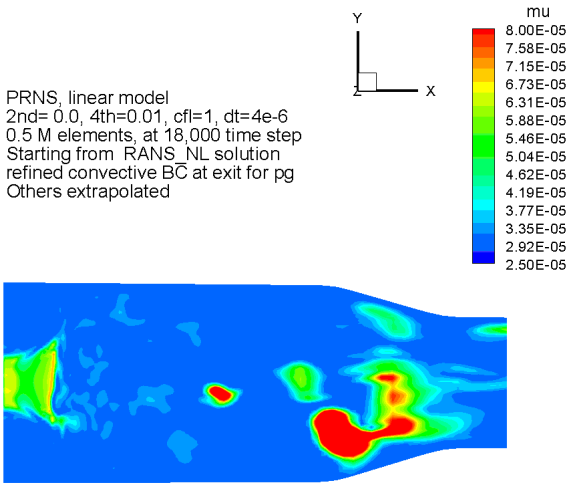

Figure 43.—Effective viscosity at 18,000 time step.

3.3 Flow in a Single-Element LDI Combustor

The lean direct injection (LDI) injector is a liquid fuel injector developed to reduce aircraft emissions. Stable combustion is essentially completed within a short distance through rapid fuel and air mixing. This design also allows for many small fuel injectors integrated into modules facilitating different fuel staging strategies, such as the one shown in Figure 44. So far, experimental observations have not fully clarified the dynamics of the mixing and combustion processes occurring in these injectors, and numerical studies need to be conducted to achieve a better understanding of the underlying unsteady physics of the LDI combustor.

A very large eddy simulation (PRNS/VLES) has been carried out for the non-reacting turbulent flow in a single-element LDI combustor as the first step towards the simulation of, for example, a 3x3 injector module.

Figure 45 depicts the single-element LDI combustor geometry and its computational domain. The numerical grid is formed using hexahedral elements and the total number of elements is about 862,000, which is a relatively coarse grid used in a previous RANS simulation (Ref. 22). Embedded in this figure are the instantaneous iso-surface of zero axial velocity component colored by the subscale effective viscosity and six instantaneous stream lines originating from the inlet of the injector, then passing through the swirler and the convergent-divergent nozzle, finally entering the combustion chamber.

In this study, we first carry out a steady RANS simulation to provide the initial flow field for the PRNS/VLES simulation. The inlet boundary condition is set by specifying the velocity, the density and the temperature based on the experimental data, the outlet boundary condition is an unsteady convective boundary condition (Ref. 19). The nonlinear subscale model is used since it has been proven to be very effective in our previous studies. The value of $f\ (RCP)$ is set to 0.4444 since the available numerical grid spacing is very coarse. We have also carried out an unsteady RANS (URANS) simulation to compare with the PRNS/VLES simulation. Available experimental data is used to assess the simulation results. It is demonstrated that, even with a RANS type of grid spacing, the PRNS/VLES approach can successfully reveal the complex unsteady turbulent structures occurring in this single-element LDI combustor. These dynamically important flow structures include the precessing vortex core (PVC) and the vortex breakdown bubble (VBB). Good comparisons of velocity components with the experimental data are also demonstrated.

Figure 44.—Configuration of a 3 x 3 LDI injector module.

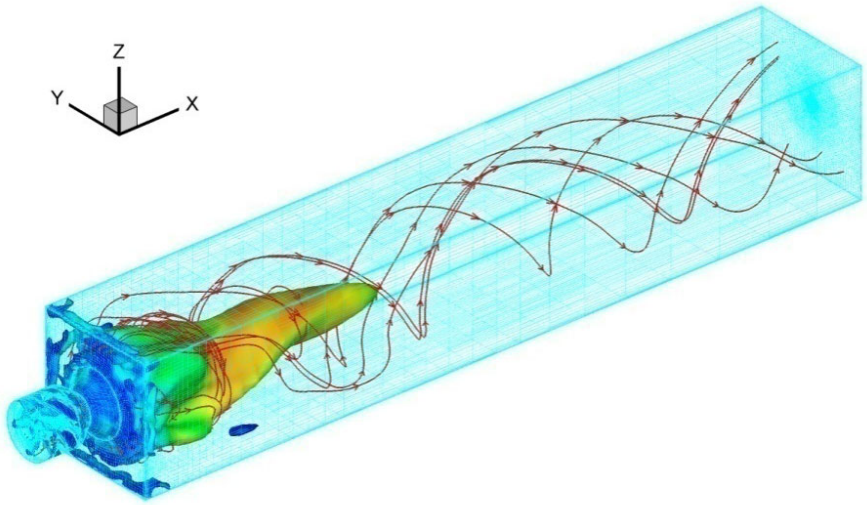

Figure 45.—A snap shot of the flow and the grid spacing.

3.3.1 Flow Structures

In the following, the instantaneous contour snap shots and the iso-surfaces of some quantities are used to illustrate the flow structures.

3.3.1.1 Instantaneous Contour Plots

Figure 46 is the contour plot of the axial velocity component in a center plane at time step 90,000. It shows that a strong recirculation zone is extended from the combustor dump plane deep into the upstream nozzle throat. Figure 47 is the contour plot of the subscale turbulent kinetic energy, which is high near the high shear regions.

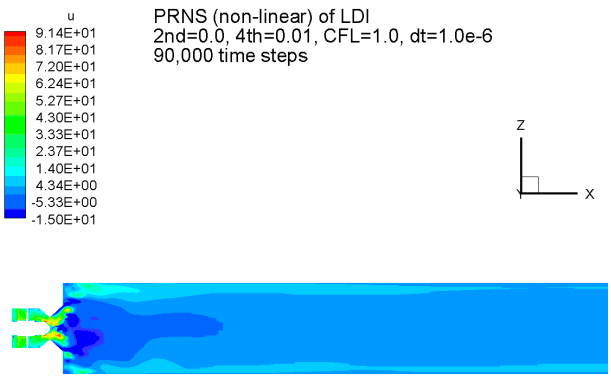

Figure 46.—Contour of axial velocity in a center plane.

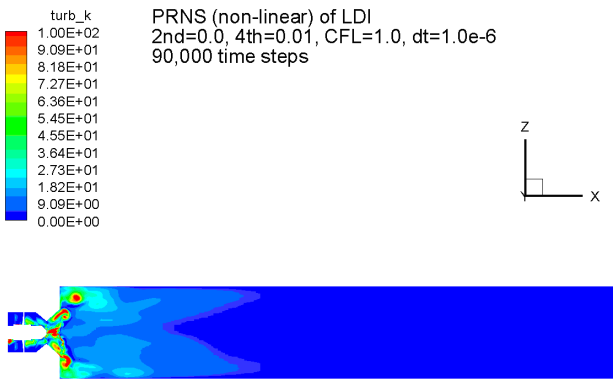

Figure 47.—Contour of subscale k in a center plane.

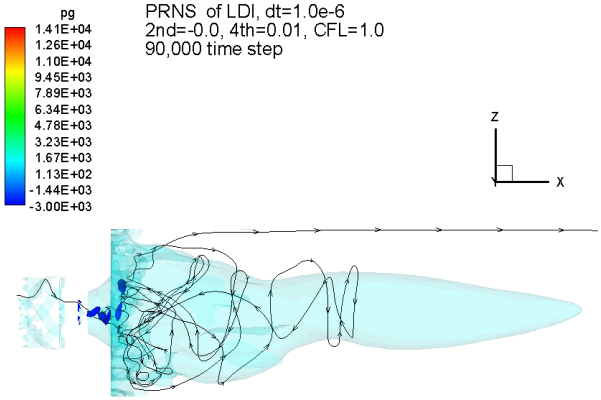

Figure 48.—Side view of the PVC and the VBB.

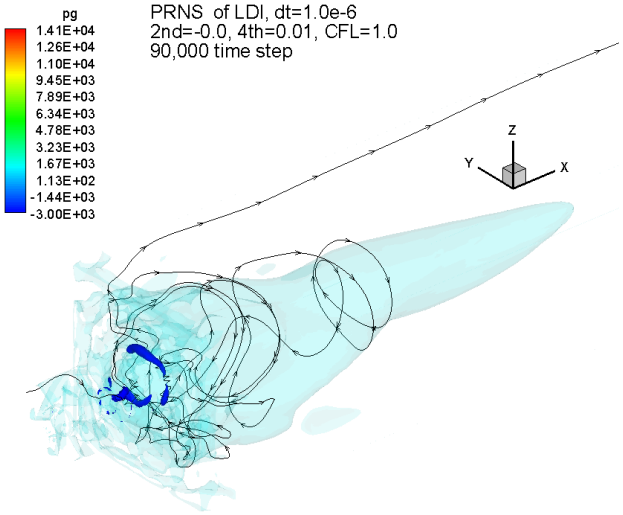

Figure 49.—Forty-five degree view of the PVC and the VBB.

3.3.1.2 Instantaneous PVC and VBB

The dominant flow structures in the LDI combustor can be best visualized via the iso-surface of the zero axial velocity and the iso-surface of a relatively low pressure. The iso-surface of the zero axial velocity is also known as the vortex breakdown bubble (VBB). The iso-surface of a sufficiently low pressure captures the precessing vortex core (PVC). Figures 48 and 49 are the snap shots taken from two different angles. Figure 48 is a side view and Figure 49 is a perspective view. In these figures, the dark blue region is a vortex core, which is formed near the nozzle throat and extends into the combustor chamber. This spiraling vortex rotates and breaks, it changes randomly in space and time. Embedded in these figures is an instantaneous stream line, which starts from the inlet of the injector and goes through a complex seemingly random path in the combustor chamber. This stream line spirals around the dark blue surface indicating that the dark blue region is indeed a vortex core. The light green surfaces are the iso-surfaces of the zero axial velocity.

3.3.2 Profiles of Velocity Components

The experimental data reported in Reference 23 is used to assess the current numerical results. The experimental data are mean values, but the numerical results are instantaneous values.

3.3.2.1 Axial Velocity Distribution Along the Centerline

Figure 50 is a comparison of the axial velocity profile between the calculated instantaneous values and the experimental mean value. Figure 51 is an enlarged view near the dump plane of the combustor chamber. These figures show that the calculated values are in a reasonable agreement with the experimental data. It also supports the experimental observation that, near the dump plane, the turbulent fluctuations are quite large.

3.3.2.2 Axial Velocity Distribution Along the y-Axis at Several Downstream Locations

The distributions of the axial velocity along the y-axis in the cross section plane at several downstream locations x = 3-, 6-, 9-, 12-, 90- and 180-mm are presented for 10 different instants and compared with the experimental mean value. Figures 52, 53 and 54 clearly indicate that the turbulent fluctuations are quite large near the inlet of the combustion chamber and are quickly reduced towards downstream as shown in Figures 55, 56 and 57. In addition, the largest turbulent fluctuations are off the centerline, somewhere between the centerline and the wall.

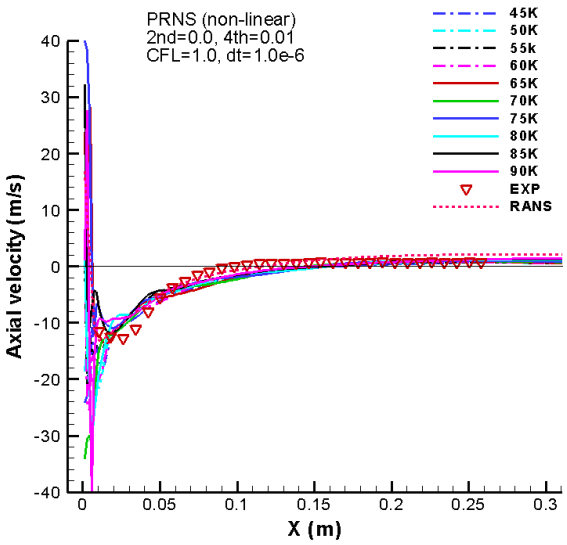

Figure 50.—Centerline profile of the axial velocity.

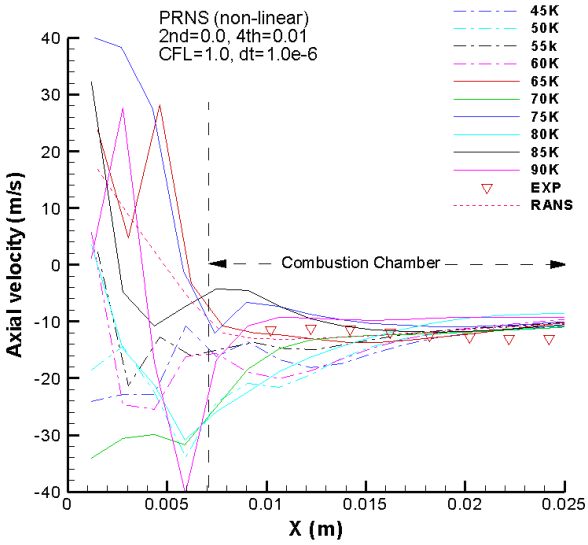

Figure 51.—Instantaneous profiles near the dump plane.

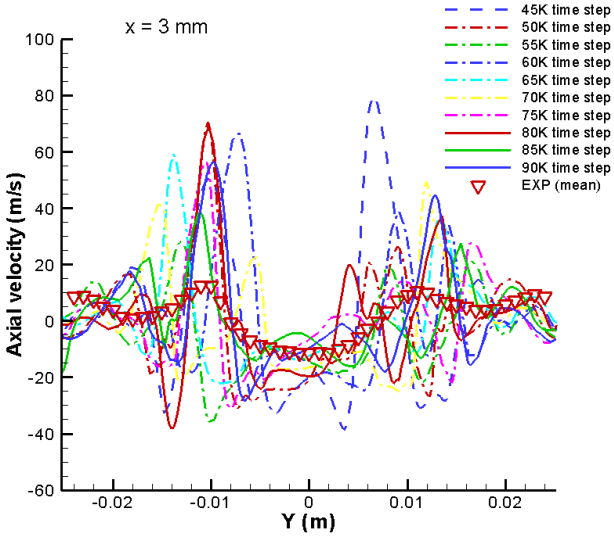

Figure 52.—Axial velocity at x = 3 mm.

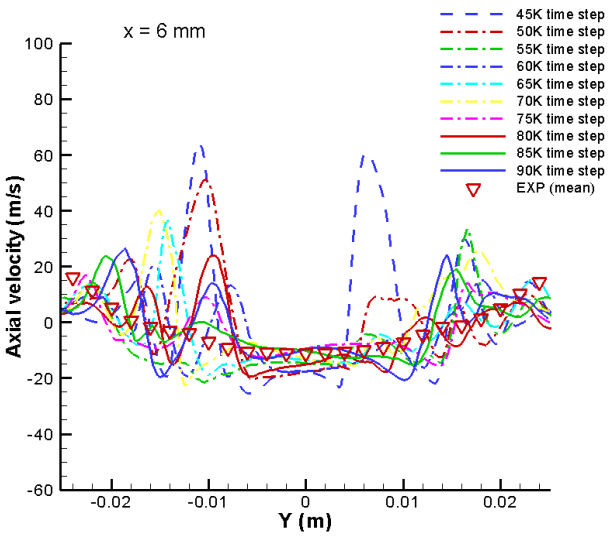

Figure 53.—Axial velocity at x = 6 mm.

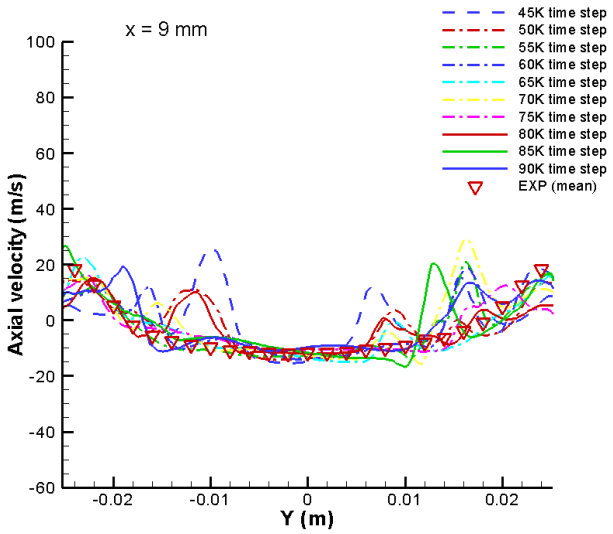

Figure 54.—Axial velocity at x= 9 mm.

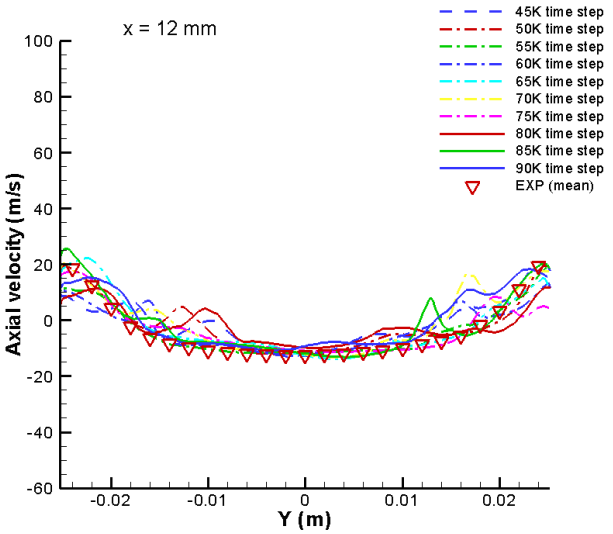

Figure 55.—Axial velocity at x = 12 mm.

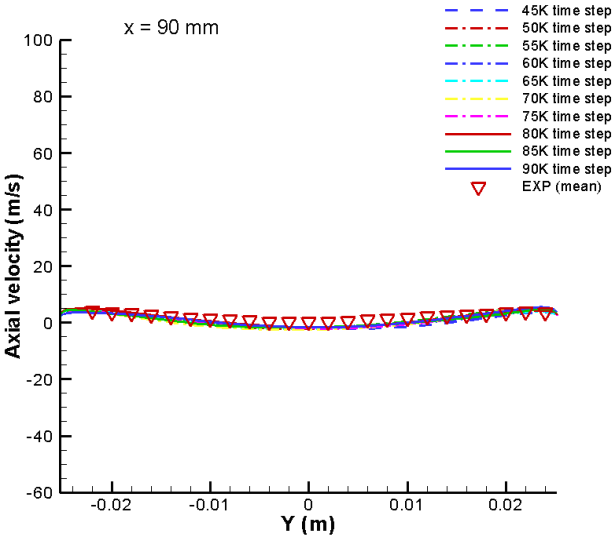

Figure 56.—Axial velocity at x = 90 mm.

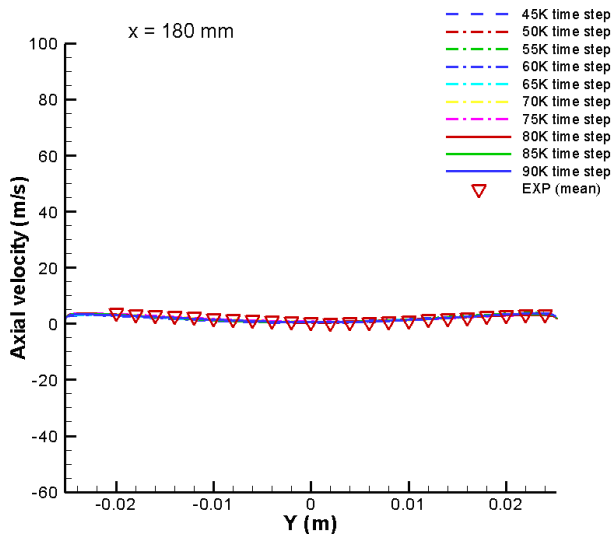

Figure 57.—Axial velocity at x = 180 mm.

3.3.2.3 Velocity Components w and v Along the y-Axis at Several Downstream Locations

The distributions of the other two velocity components w and v along the y-axis in the cross section at several downstream locations x = 3-, 6-, 9-, 12-, 15- and 90-mm are shown for 10 different instants and compared with the experimental mean value in Figures 58 to 69. Again, these figures clearly indicate that the turbulent fluctuations are larger near the inlet of the combustor chamber and are quickly reduced downstream. The strongest turbulent fluctuations are found off the centerline, somewhere between the centerline and the wall.

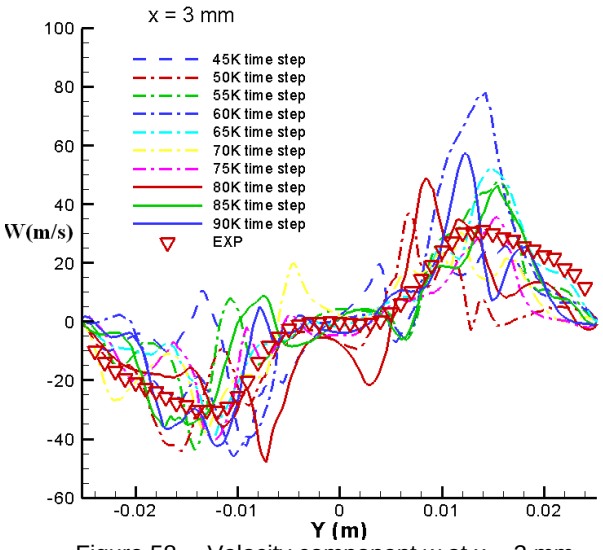

Figure 58.—Velocity component w at x = 3 mm.

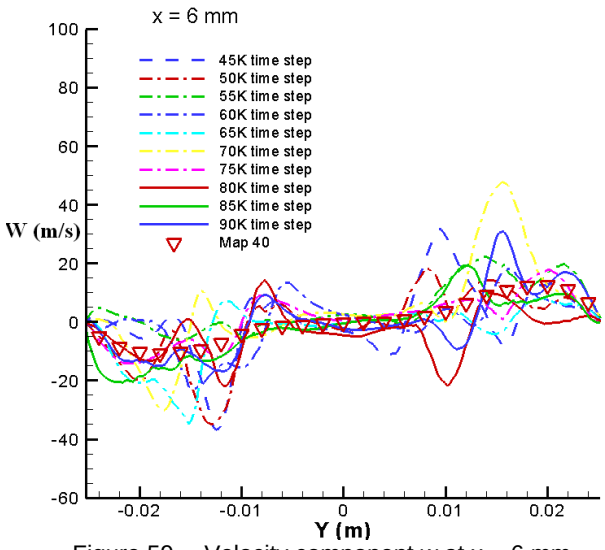

Figure 59.—Velocity component w at x = 6 mm.

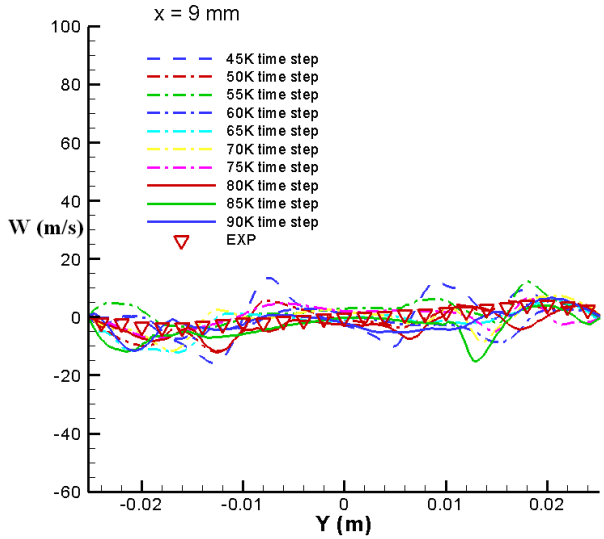

Figure 60.—Velocity component w at x = 9 mm.

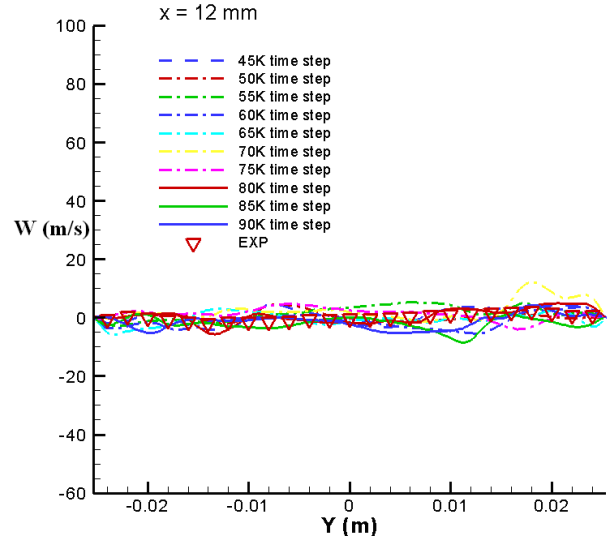

Figure 61.—Velocity component w at x = 12 mm.

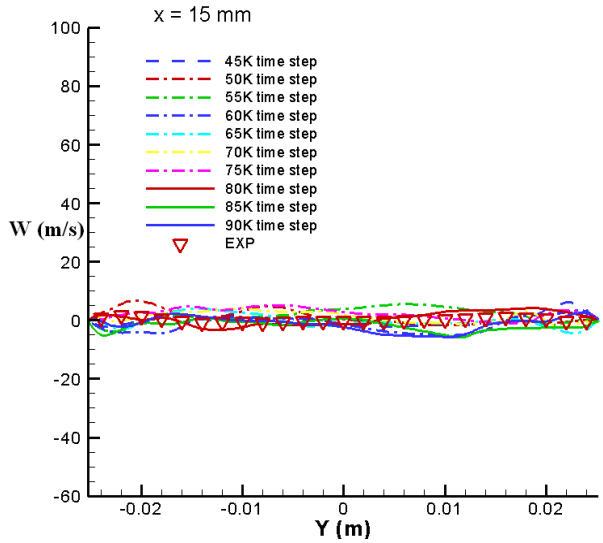

Figure 62.—Velocity component w at x = 15 mm.

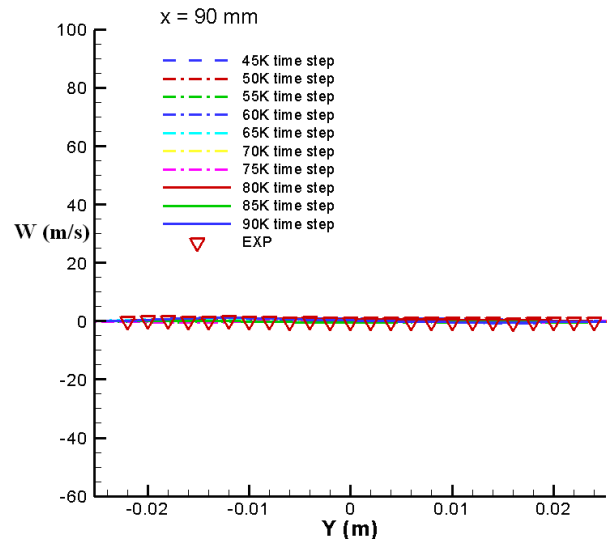

Figure 63.—Velocity component w at x = 90 mm.

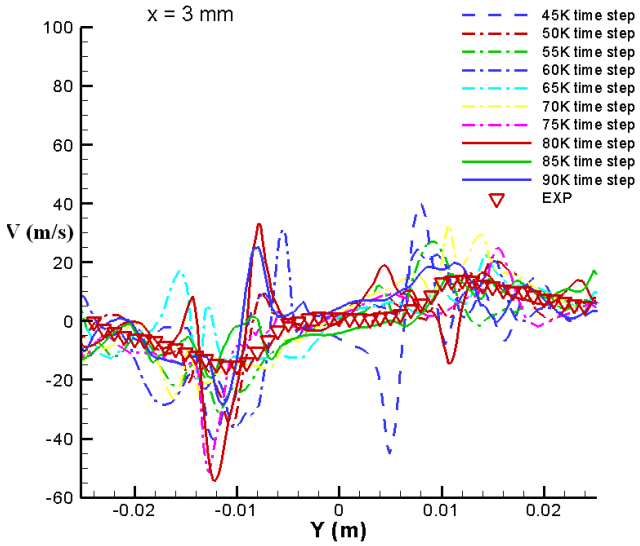

Figure 64.—Velocity component v at x = 3 mm.

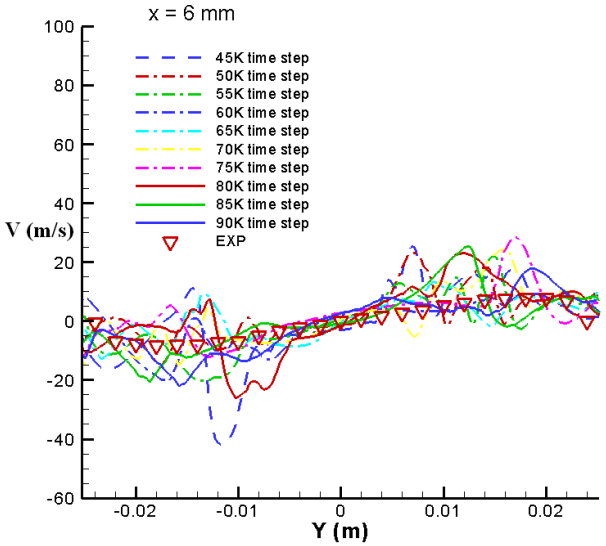

Figure 65.—Velocity component v at x = 6 mm.

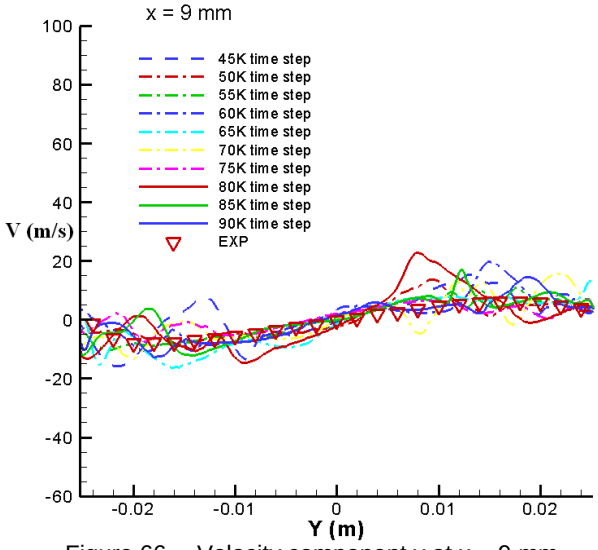

Figure 66.—Velocity component v at x = 9 mm.

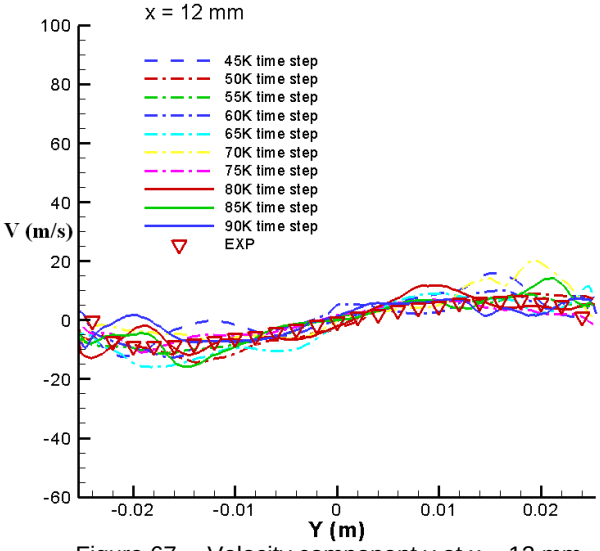

Figure 67.—Velocity component v at x = 12 mm.

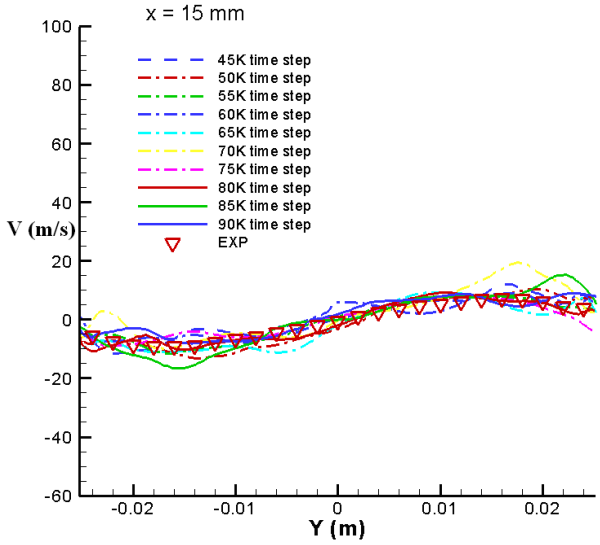

Figure 68.—Velocity component v at x = 15 mm.

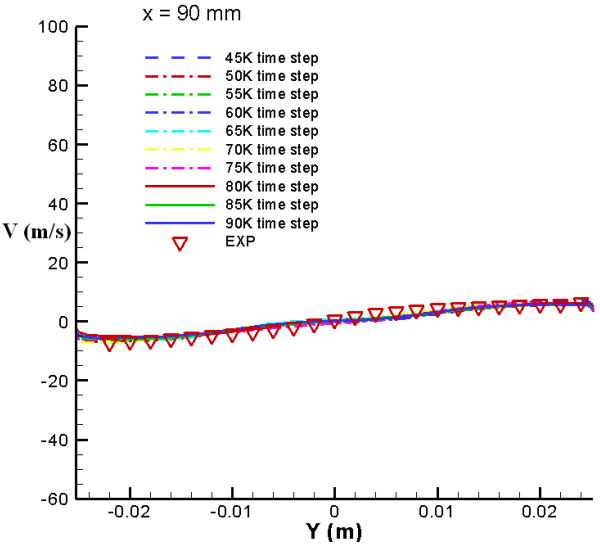

Figure 69.—Velocity component v at x = 90 mm.

3.3.3 Comparisons Between RANS, URANS, PRNS/VLES and Experimental Data

This section will compare some time averaged mean velocity profiles from PRNS/VLES simulation. The mean values are obtained by time averaging the PRNS/VLES simulation over the last 10,000 time steps.

3.3.3.1 Axial Mean Velocity Along the y-Axis at Several Downstream Locations

The distributions of the axial mean velocity along the y-axis in the cross section plane at several downstream locations x = 3-, 6-, 9-, 12-, 90- and 180-mm are presented for RANS, URANS and PRNS/VLES and compared with the experimental mean values. Figures 70 to 75 clearly show that the time averaged axial velocity profile from PRNS/VLES simulation are much closer to the experimental data, especially in the region near the inlet of the combustor chamber where turbulent fluctuations are strong.

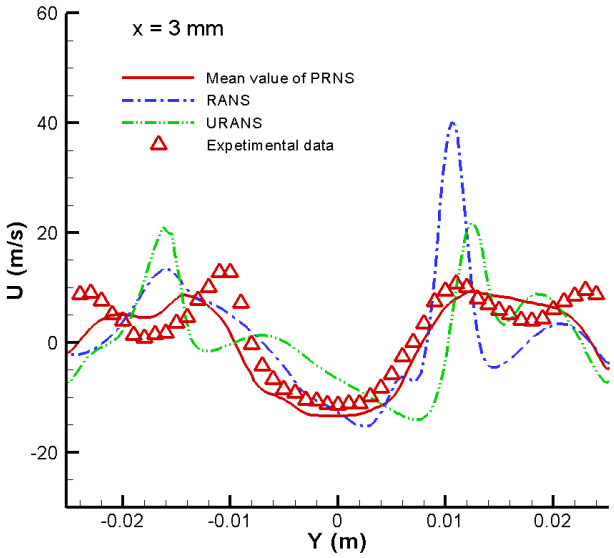

Figure 70.—Velocity component U at x = 3 mm.

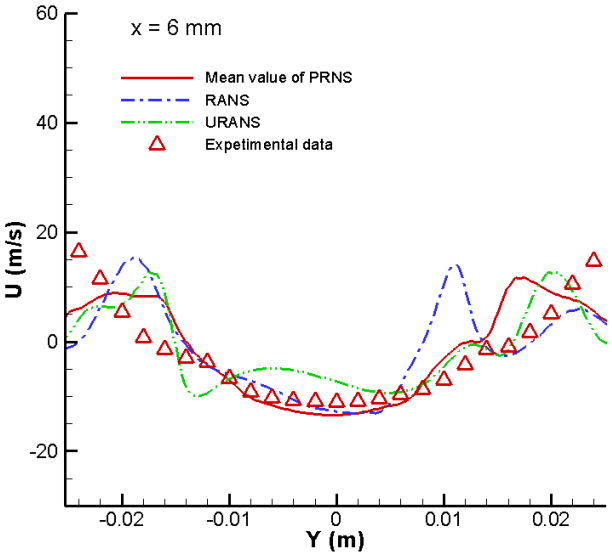

Figure 71.—Velocity component U at x = 6 mm.

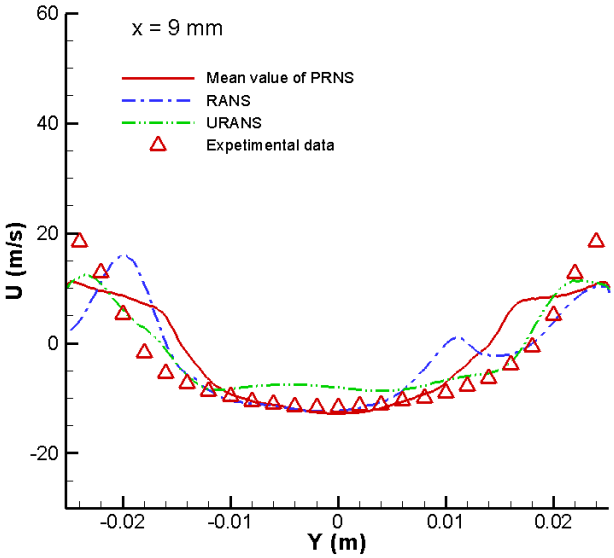

Figure 72.—Velocity component U at x = 9 mm.

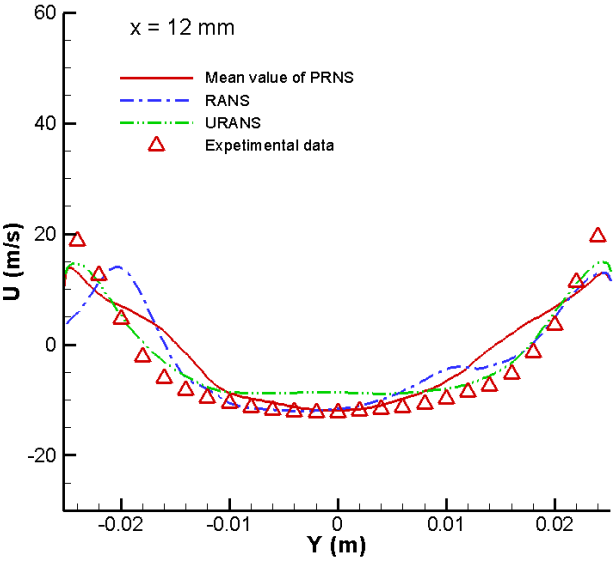

Figure 73.—Velocity component U at x = 12 mm.

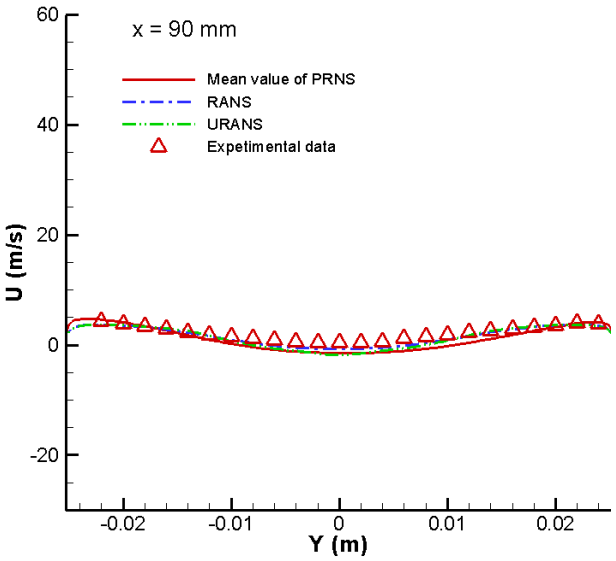

Figure 74.—Velocity component U at x = 90 mm.

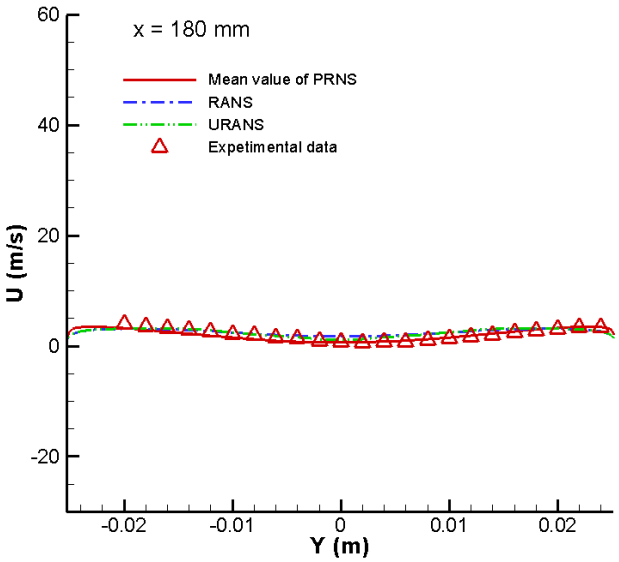

Figure 75.—Velocity component U at x = 180 mm.

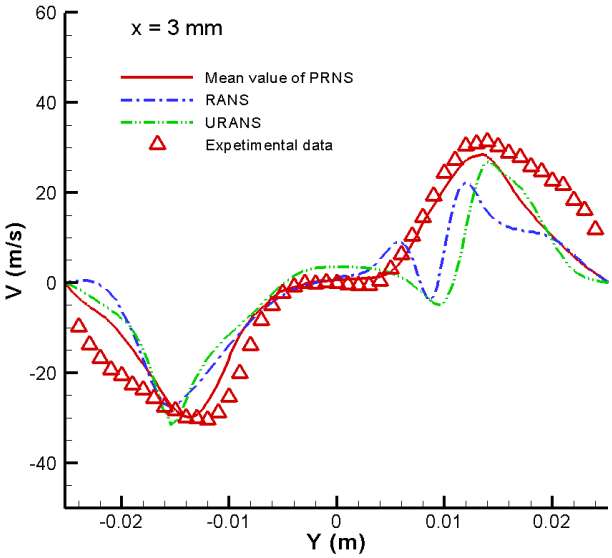

Figure 76.—Velocity component V at x = 3 mm.

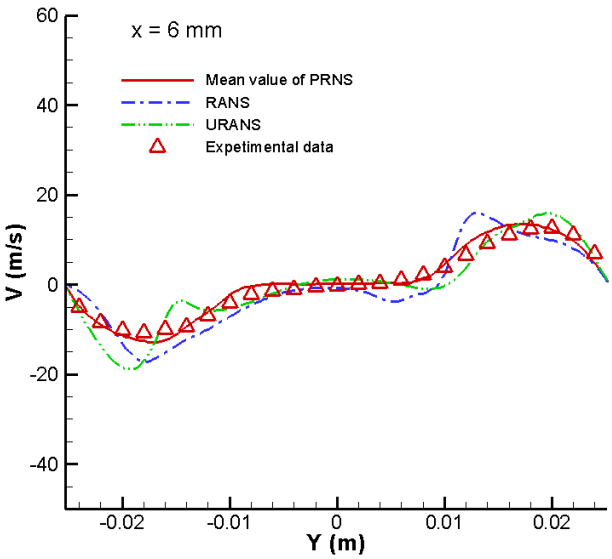

Figure 77.—Velocity component V at x = 6 mm.

3.3.3.2 Mean Velocity Components w and v Along the y-Axis at Several Downstream Locations

The distributions of the other two mean velocity components w and v along the y-axis in the cross section at several downstream locations x = 3-, 6-, 9-, 12-, 15- and 90-mm are compared with the experimental mean value in Figures 76 to 87. Again, these figures clearly indicate that the time averaged mean velocity profiles from PRNS/VLES simulation are much closer to the experimental data, especially in the region near the inlet of the combustor chamber where turbulent fluctuations are strong.

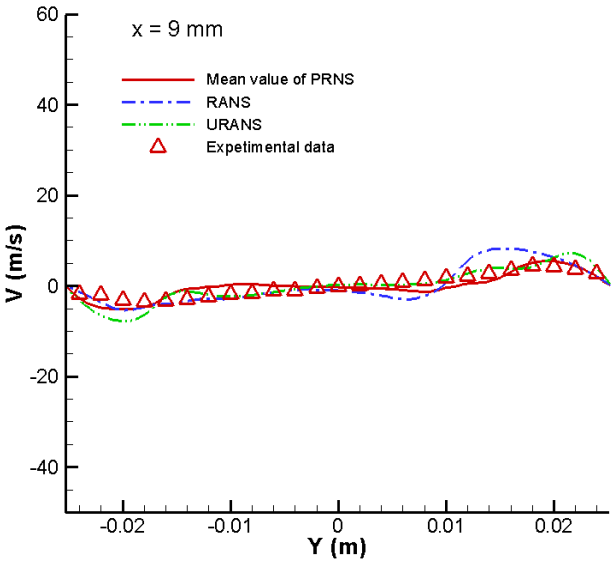

Figure 78.—Velocity component V at x = 9 mm.

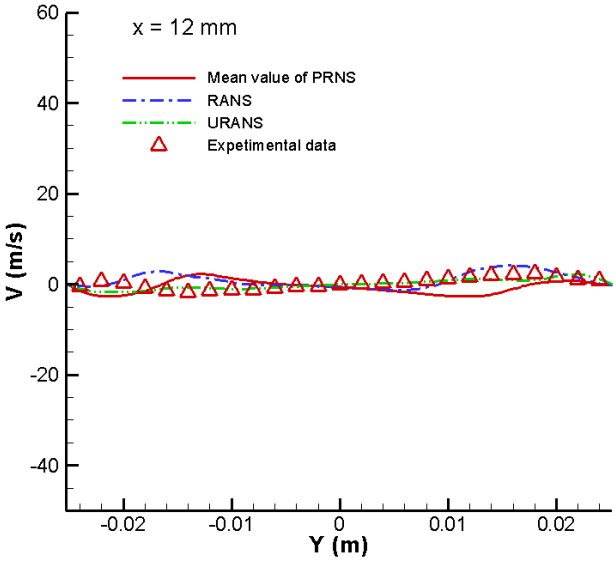

Figure 79.—Velocity component V at x = 12 mm.

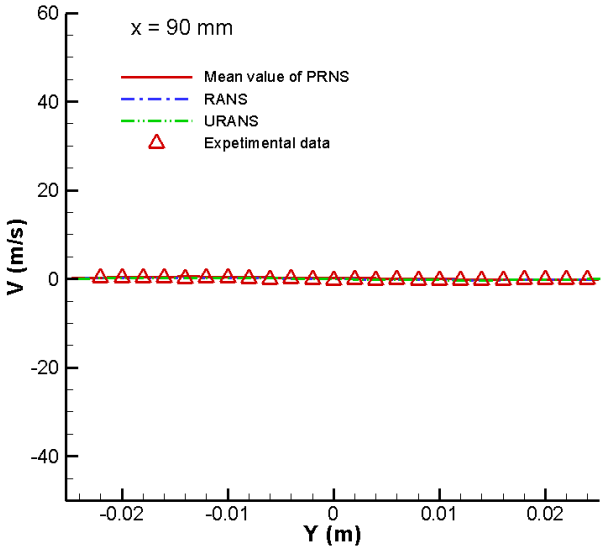

Figure 80.—Velocity component V at x = 90 mm.

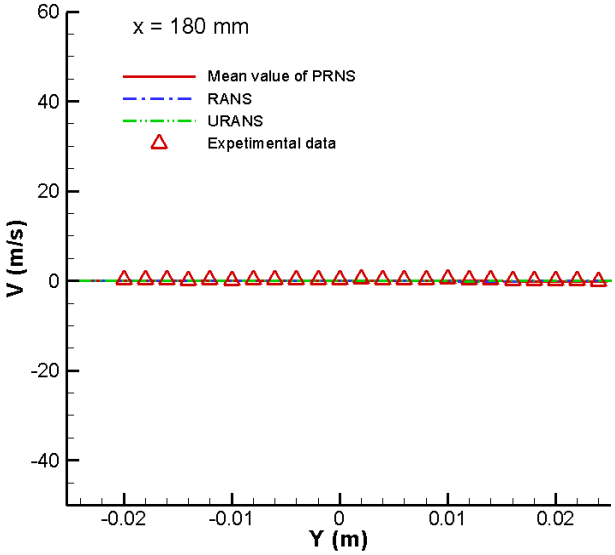

Figure 81.—Velocity component V at x = 180 mm.

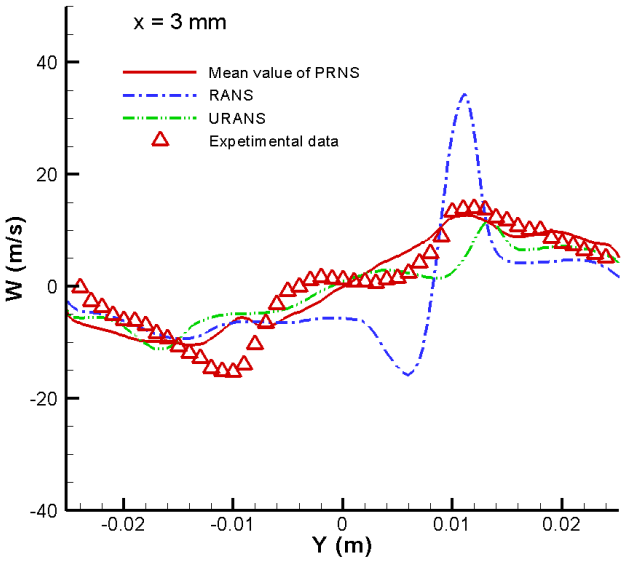

Figure 82.—Velocity component w at x = 3 mm.

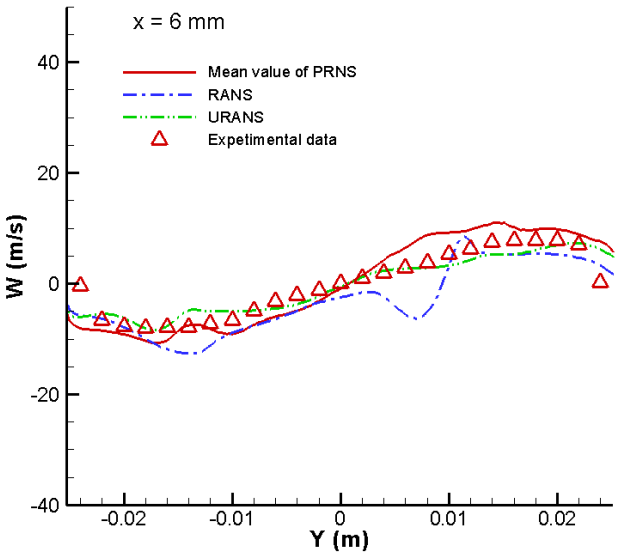

Figure 83.—Velocity component w at x = 6 mm.

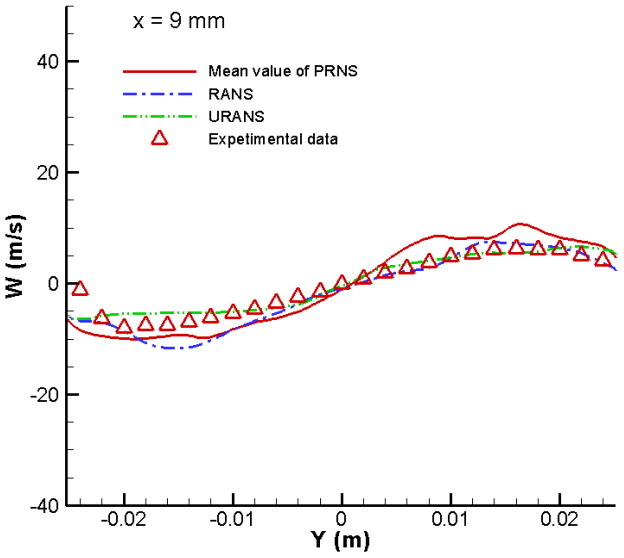

Figure 84.—Velocity component w at x = 9 mm.

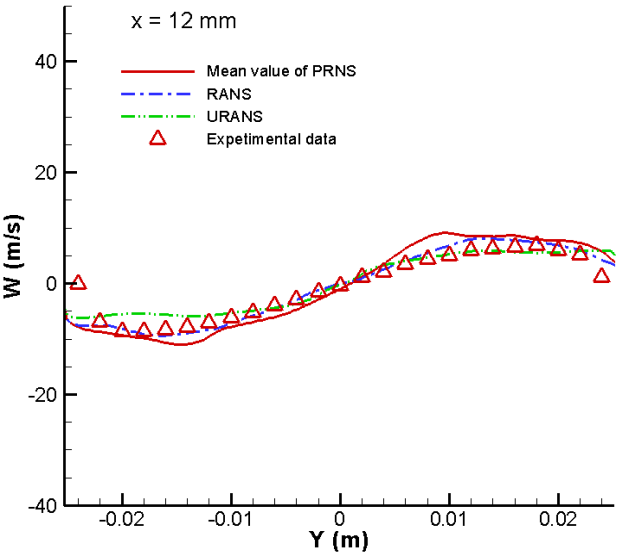

Figure 85.—Velocity component w at x = 12 mm.

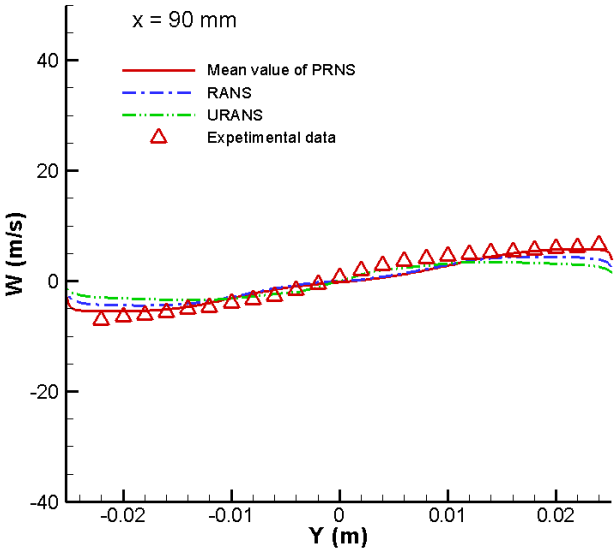

Figure 86.—Velocity component w at x = 90 mm.

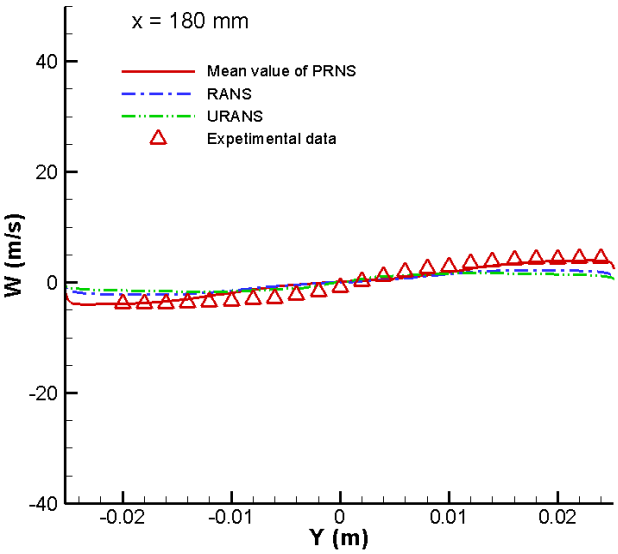

Figure 87.—Velocity component w at x = 180 mm.

4.0 Conclusions

The basic equations of the PRNS/VLES approach for the large or very large simulation are presented. They are based on the temporal filtering with a constant filter width. Consequently, they are grid-spacing independent or grid invariant. This feature allows the possibility of achieving a grid independent solution.

The nonlinear subscale model is mathematically and physically more sound than the pure eddy viscosity model. The advantage of the nonlinear subscale model over the eddy viscosity model has been demonstrated in the simulations of the turbulent pipe flow at low Reynolds number Re τ = 180 and the highly swirling flow issued from a LM6000 single injector. In both cases, the pure eddy viscosity model does not lead to a sustainable and physically meaningful solution.

The simulations of the single-element LDI injector flow using the nonlinear subscale model has demonstrated that the PRNS/VLES approach can capture the dynamically important unsteady turbulent structures even with a grid spacing typically used in the RANS calculation. This is particularly encouraging, because the capability of revealing unsteady turbulent flow structures with a coarse grid is very much desired for the practical engineering application.

References

1. Liu, N.-S., and Shih, T.-H., "Turbulence Modeling for Very Large-Eddy Simulation," *AIAA Journal,* Vol. 44, No. 4, 2006, pp. 687-697.
2. Shih, T.-H., and Liu, N.-S., "Modeling of Internal Reacting Flows and External Static Stall flows Using RANS and PRNS," Flow, Turbulence and Combust (2008) 81:279-299.
3. Davidson, L., and Peng, S.H., "Hybrid LES-RANS modeling: a one-equation SGS model combined with a k – ω model for predicting re-circulating flows," International Journal for Numerical Methods in Fluids, Vol.43, 2003, pp. 1003-1018.
4. Larsson, J., Lien, F. S. and Yee, E., "The artificial buffer layer and the effect of forcing in hybrid LES/RANS," International Journal of Heat and Fluid Flow, Vol. 28, 2007, pp. 1443-1459.
5. Spalart, P.R., Jou, W.H., and Allmaras, S.R., "Comments on the feasibility of LES for wings and on a hybrid RANS/LES approach," Advances in DNS/LES, 1997, Greyden Press.
6. Fasel, H.F., von Terzi, D.A., and Sandberg, R.D., "A methodology for simulating compressible turbulent flows," Journal of Applied Mechanics, Vol. 73, May 2006, pp. 405-412.

7. Cabot, W. and Moin, P., "Approximate wall boundary conditions in the large-eddy simulation of high Reynolds number flow," Flow, Turbulence and Combustion, Vol. 63, January 2000, pp. 269-291.
8. Sagaut, P., "Large eddy simulation for incompressible flows," 2006, Springer-Verlag.
9. Shih, T.-H., "Constitutive Relations and Realizability of Single-Point Turbulence Closures" Turbulence and Transition Modelling, Chapter 4, Edited by Hallback, M., Henningson, D.S., Johansson, A.V. and Alfredsson, P.H., KLUWER ACADEMIC PUBLISHERS, 1996.
10. Shih, T.-H., "Mathematical Modeling of Turbulent Flows," Fluid Dynamics Research Vol. 20 (1997), H. Daiguji, Y Miyake, N. Kasagi.
11. Smagorinsky, J., "General Circulation Experiments with the Primitive Equations," Month. Weath. Rev., Vol. 93, 1963, pp. 99-165.
12. Kim, W-W., Menon, S., and Mongia, H.C., "Large Eddy Simulation of Gas Turbine Combustor Flow," Combust. Sci. and Tech., Vol. 143, 1999, pp. 25-62.
13. Shih, T.-H., Zhu, J., Liou, W., Chen, K-H., Liu, N-S., and Lumley, J.L., "Modeling of turbulent swirling flows," NASA/TM 1997-113112, 1997.
14. Shih, T.-H., Liou, W.W., Shabbir, A., Yang, Z., and Zhu, J., "A New $k-\varepsilon$ Eddy Viscosity Model for High Reynolds Number Turbulent Flows," Computers Fluids, Vol. 24, No. 3, 1995, pp. 227-238.
15. Tennekes H. and Lumley J. L., A First Course in Turbulence, the MIT Press, 1972.
16. Zagarola, M.V., and Smith, A.J., "Experiments in High Reynolds Number Turbulent Pipe Flow," Phys. Rev. Lett. 78, 1997.
17. Shih, T.-H. and Liu, N.-S., "Assessment of the Partially Resolved Numerical Simulation (PRNS) Approach in the National Combustion Code (NCC) for Turbulent Nonreacting and Reacting Flows," NASA/TM 2008-215418, 2008.
18. Shih, T.-H., Povinelli, L.A., and Liu, N.-S., "Application of Generalized Wall Function for Complex Turbulent Flows," J. of Turbulence, 4 (2003) 015.
19. Shih, T.-H. and Liu, N.-S., "Numerical Study of Outlet Boundary Conditions for Unsteady Turbulent Internal Flows Using the NCC," NASA/TM—2009-215486, 2009.
20. Ferziger, J. H. and Milovan, P., Computational Methods for Fluid Dynamics. Springer, 1996.
21. Grinstein, F. F., Oran, E. S. and Boris, J. P.," Pressure field, feedback, and global instabilities of subsonic spatially developing mixing layers," Phys. Fluids A 3 (10), October 1991.
22. Davoudzadeh, F., Liu, N.-S. and Moder, J. P., "Investigation of Swirling Air Flows Generated by axial Swirlers in a Flame Tube," Proceedings of GT2006 ASME Turbo Expo 2006: Power for Land, Sea, and Air May 8-11, 2006, Barcelona, Spain.
23. Cai, J., Jeng, S.-M., and Tacina, R., "The Structure of A Swirl-Stabilized Reacting Spray Issued from An Axial Swirler," AIAA-2005-1424, 43rd AIAA Aerospace Science Meeting and Exhibit, 10-13 January 2005, Reno, NV.

REPORT DOCUMENTATION PAGE	Form Approved OMB No. 0704-0188

1. REPORT DATE *(DD-MM-YYYY)*	2. REPORT TYPE	3. DATES COVERED *(From - To)*
01-05-2010	Technical Memorandum	

4. TITLE AND SUBTITLE
A Nonlinear Dynamic Subscale Model for Partially Resolved Numerical Simulation (PRNS)/Very Large Eddy Simulation (VLES) of Internal Non-Reacting Flows

5a. CONTRACT NUMBER

5b. GRANT NUMBER

5c. PROGRAM ELEMENT NUMBER

6. AUTHOR(S)
Shih, Tsan-Hsing; Liu, Nan-Suey

5d. PROJECT NUMBER

5e. TASK NUMBER

5f. WORK UNIT NUMBER
WBS 561581.02.08.03.16.02

7. PERFORMING ORGANIZATION NAME(S) AND ADDRESS(ES)
National Aeronautics and Space Administration
John H. Glenn Research Center at Lewis Field
Cleveland, Ohio 44135-3191

8. PERFORMING ORGANIZATION REPORT NUMBER
E-17257

9. SPONSORING/MONITORING AGENCY NAME(S) AND ADDRESS(ES)
National Aeronautics and Space Administration
Washington, DC 20546-0001

10. SPONSORING/MONITOR'S ACRONYM(S)
NASA

11. SPONSORING/MONITORING REPORT NUMBER
NASA/TM-2010-216323

12. DISTRIBUTION/AVAILABILITY STATEMENT
Unclassified-Unlimited
Subject Categories: 01 and 64
Available electronically at http://gltrs.grc.nasa.gov
This publication is available from the NASA Center for AeroSpace Information, 443-757-5802

13. SUPPLEMENTARY NOTES

14. ABSTRACT
A brief introduction of the temporal filter based partially resolved numerical simulation/very large eddy simulation approach (PRNS/VLES) and its distinct features are presented. A nonlinear dynamic subscale model and its advantages over the linear subscale eddy viscosity model are described. In addition, a guideline for conducting a PRNS/VLES simulation is provided. Results are presented for three turbulent internal flows. The first one is the turbulent pipe flow at low and high Reynolds numbers to illustrate the basic features of PRNS/VLES; the second one is the swirling turbulent flow in a LM6000 single injector to further demonstrate the differences in the calculated flow fields resulting from the nonlinear model versus the pure eddy viscosity model; the third one is a more complex turbulent flow generated in a single-element lean direct injection (LDI) combustor, the calculated result has demonstrated that the current PRNS/VLES approach is capable of capturing the dynamically important, unsteady turbulent structures while using a relatively coarse grid.

15. SUBJECT TERMS
Very large eddy simulation; CFD

16. SECURITY CLASSIFICATION OF:			17. LIMITATION OF ABSTRACT	18. NUMBER OF PAGES	19a. NAME OF RESPONSIBLE PERSON
a. REPORT	b. ABSTRACT	c. THIS PAGE			STI Help Desk (email:help@sti.nasa.gov)
U	U	U	UU	43	19b. TELEPHONE NUMBER *(include area code)* 443-757-5802